PAPER

# Localized radial bumps of a neural field equation on the Euclidean plane and the Poincaré disc

IOP PUBLISHING NONLINEARITY

Nonlinearity **26** (2013) 437–478 doi:10.1088/0951-7715/26/2/437

# Localized radial bumps of a neural field equation on the Euclidean plane and the Poincaré disc

**Grégory Faye**[1,2], **James Rankin**[2] **and David J B Lloyd**[3]

[1] School of Mathematics, University of Minnesota, Minneapolis, USA
[2] NeuroMathComp Project Team, Inria, Sophia Antipolis, France
[3] Department of Mathematics, University of Surrey, Guilford, GU2 7XH, UK

Received 25 June 2012, in final form 23 November 2012
Published 2 January 2013
Online at stacks.iop.org/Non/26/437

Recommended by J A Glazier

**Abstract**

We analyse radially symmetric localized bump solutions of an integro-differential neural field equation posed in Euclidean and hyperbolic geometry. The connectivity function and the nonlinear firing rate function are chosen such that radial spatial dynamics can be considered. Using integral transforms, we derive a partial differential equation for the neural field equation in both geometries and then prove the existence of small amplitude radially symmetric spots bifurcating from the trivial state. Numerical continuation is then used to path follow the spots and their bifurcations away from onset in parameter space. It is found that the radial bumps in Euclidean geometry are linearly stable in a larger parameter region than bumps in the hyperbolic geometry. We also find and path follow localized structures that bifurcate from branches of radially symmetric solutions with $D_6$-symmetry and $D_8$-symmetry in the Euclidean and hyperbolic cases, respectively. Finally, we discuss the applications of our results in the context of neural field models of short term memory and edges and textures selectivity in a hypercolumn of the visual cortex.

Mathematics Subject Classification: 35B22; 37G05; 92B20

(Some figures may appear in colour only in the online journal)

## 1. Introduction

A popular approach for understanding coarse-grained activity of large ensembles of neurons in cortex is to model cortical space as continuous. This natural approximation, based on the pioneering work of Wilson and Cowan [99, 100] and Amari [1, 2], gives rise to the notion of neural field models. These models typically take the form of integro-differential equations that describe the evolution of macroscopic variables such as the firing rate activity or average membrane voltage of populations of neurons. Unlike spiking neural network

  

models, neural field models have the advantage that analytic techniques for partial differential equations (PDEs) can be adapted to study their nonlinear dynamics with a small set of parameters. Various types of dynamical behaviour have been observed in neural field models ranging from spatially and temporally periodic patterns [17, 36, 40, 64, 92], localized regions of activity [67, 73] to traveling waves [49, 50, 66, 74, 86]. Neural field equations have also successfully been used to model a wide range of neurobiological phenomena such as visual hallucinations [20, 21, 40, 45, 52], mechanisms for short term memory [38, 46, 56, 57, 72, 73] and feature selectivity in the visual cortex [14, 16, 19, 48, 58].

In this paper, we consider the canonical Wilson–Cowan–Amari neural field equation [1, 100] that describes the evolution of the average membrane voltage of a neuronal population, $u(\boldsymbol{r}, t)$, given by

$$\kappa \partial_t u(\boldsymbol{r}, t) = -u(\boldsymbol{r}, t) + \int_\Omega W(\boldsymbol{r}, \boldsymbol{r}') S(u(\boldsymbol{r}', t)) \mathrm{dm}(\boldsymbol{r}') \tag{1.1}$$

where $\kappa$ is a temporal constant, that we set equal to one for mathematical simplicity, and $\Omega$ can either model physical space on the cortex (cortical space) or an abstracted feature space with the corresponding measure $\mathrm{dm}(\cdot)$. The use of an abstracted feature space provides a convenient way to represent features for which neuronal populations have some spatially distributed selectivity such as orientation [14], direction [84] or textures [26]. The firing rate function $S$ is generally chosen to be either a Heaviside step function [1, 32, 87], a piecewise linear function [56, 57] or a smooth function of sigmoidal type [31, 38, 42, 73]. The coupling of the neurons, described by the connectivity function $W$, is typically assumed to have a so-called 'Mexican hat' or so-called 'wizard hat' shape, although strictly positive connectivity functions have also been considered in, for example, [88]. The precise form of the connectivity function is often chosen such that a Fourier transform can be applied to (1.1) to yield a PDE; such an approach goes back to the work of Jirsa and Haken in [63] and has been used by a number of other authors [31, 72, 73].

When considering cortical space, $\Omega$ is taken to be a subset of $\mathbb{R}^d$ with $d = 1, 2$ or 3 and naturally inherits a Euclidean geometry. For $\Omega = \mathbb{R}$, the most widely studied case, various analyses have found a range of solutions of (1.1) from localized states [32, 46, 56, 57, 73] to spatially periodic [6, 7, 30, 61]. However, the case $\Omega = \mathbb{R}$ is of limited biological interest since the visual cortex is inherently a three-dimensional object. Fortunately, a piece of cortex can be well approximated by a sheet as its thickness is much smaller than the other directions and this has lead various studies to look at the case where $\Omega = \mathbb{R}^2$; see for instance [32, 49, 50, 64, 72, 85, 93, 98]. Recently, there has also been much interest in studying equation (1.1) in other Riemannian geometries such as hyperbolic geometry where $\Omega$ can be taken to be the Poincaré disc $\mathbb{D}$[4] and the neural field equation now models edge and texture selectivity in the visual cortex [26, 48]. Only periodic solutions in the Poincaré disc have so far been investigated by Chossat and Faye [27, 47].

In the case of Euclidean geometry with a Heaviside firing function $S$, it is possible to explicitly construct general radially symmetric bump solutions to equation (1.1); see [33, 50, 85, 93, 98]. While this approach allows one to construct closed form formulae for the solutions, it has the drawback that it does not explain the nucleation, from a dynamical point of view, of radially symmetric bumps with a more realistic firing rate such as a smooth sigmoidal function.

The first study with more realistic firing function was carried out by Laing *et al* [38, 72, 73] on both the real line and the Euclidean plane where numerical continuation methods have been used to path follow localized solutions. In the previous studies of Laing *et al* , spatial dynamics

[4] $\mathbb{D} = \{z \in \mathbb{C} \mid 0 \leqslant |z| < 1\}$.

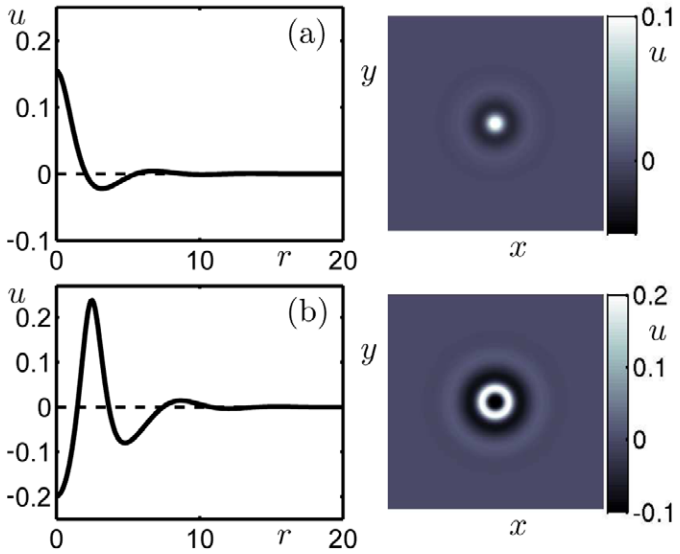


**Figure 1.** Examples of spot solutions as computed for the neural field equations, which are solutions to (3.7); see sections 3.1.3 and 4 for further details. (*a*) Spot A solution that exists for $\widehat{W}_c = 5$, $\mu = 6$. (*b*) Coexisting spot B solution. Each solution is visualized through a 1D slice (left) and a pseudocolor plot in the Euclidean plane (right).

methods cannot be used to prove the existence of localized states due to the non-analyticity of the chosen firing rate function. A bifurcation analysis for more general analytic firing rate function was recently carried out by Faye *et al* [46] where they were able to perform normal form analysis in one dimension near a Turing instability and describe the nucleation process of localized patterns. Furthermore, Faye *et al* [46] found that the bifurcating pulses underwent homoclinic snaking away from onset similar to that seen in the Swift–Hohenberg equation; see [23, 35, 101] for a discussion of homoclinic snaking.

Most choices of connectivity functions lead to a PDE (via a Fourier transform) whose stationary states satisfy a 'Swift–Hohenberg'-type PDE [46, 63, 72, 73]. Recently, there has been much progress made in understanding localized patterns in the Swift–Hohenberg equation on the plane where various planar (cellular hexagon, square and roll) fronts and fully localized two-dimensional patches have been investigated; we note that similar hexagonal patches have been computed in (1.1) by Laing and Troy [72]. For one-dimensional and planar localized patterns, a detailed geometric dynamical systems theory has been developed to explain the intricate bifurcation structure of such patterns [13, 24, 68, 69]. Unfortunately, the geometric theory breaks down for fully localized two-dimensional patches and only numerical studies exist. However, for the Swift–Hohenberg equation near the Turing instability, three types of small amplitude radially symmetric localized solutions have been proven to exist: a localized ring decaying to almost zero at the core, a spot with a maximum at the origin (called spot A; see figure 1(*a*)) and a spot with minimum at the origin (called spot B; see figure 1(*b*)); see [77, 80–82]. The proofs rely on matching, at $O(1/r^2)$, the 'Core' manifold that describes solutions that remain bounded near $r = 0$ with the 'far-field' manifold that describes how solutions decay to the trivial state for large $r$. The Core manifold is found by carrying out an asymptotic expansion involving Bessel functions while the far-field manifold is calculated by carrying out a radial normal form expansion near $r = \infty$. The main technical difficulty is that the far-field normal form is only valid down to $O(1/r)$ and so the manifold has to be

carefully followed until $O(1/r^2)$. Localized rings occur due to a localized pulse in the far-field normal form equations and require that the bifurcation of rolls at $r = \infty$ is subcritical. Spot A solutions occur due to the unfolding of a quadratic tangency of the core manifold and the cubic tangency of the far-field manifold with the trivial state at onset; see [77, figure 4]. The spot B state is formed by 'gluing' the spot A and localized ring solution. Crucially, all these localized radial states are $L^2$-functions that cannot be found via a straightforward Lyapunov–Schmidt reduction. In this article, we will only be interested in the existence of spot A type of solutions for the neural field equation (1.1) as these localized solutions are the most relevant from a neuroscience point of view. Indeed, in many experimental studies [29, 51, 83], localized regions of cortical activity closely resemble a spot A solution with the shape of a $J_0(r)$-Bessel function at the core with no ring structure. For the localized ring and spot B proofs one requires an additional hypothesis that the stable and unstable manifolds of the ring solution in the far-field normal form transversely intersect; see [82]. Spot B and localized rings have not been observed experimentally and we shall not discuss these further. From now on we shall use the terms spot and bump interchangeably to refer to the spot A states.

The main aim of this paper is to prove the existence of radially symmetric localized solutions for the neural field equation (1.1) in the case where $\Omega$ is equal to either $\mathbb{R}^2$ or $\mathbb{D}$ with a general analytic firing rate function. We will show that the existence proof of spot (spot A) solutions in the Swift–Hohenberg equation (in Euclidean geometry) can be adapted to finding radial spots in (1.1) in both Euclidean and hyperbolic geometry and hence we present both proofs together. These existence results provide a starting point for a numerical investigation of other fully localized patterns that bifurcate off the radial spots and are of interest from a biological point of view.

The spot existence proofs in the Euclidean case are a straightforward adaption of those for the Swift–Hohenberg equation and provide the basic ideas for the existence proof in the hyperbolic case. Two major problems need to be overcome in order to prove the existence of spot A solutions in the hyperbolic case. Firstly, one needs to define a suitable connectivity function and integral transform such that a PDE can be derived where radial spatial dynamics can be considered. Recently, Faye [43] showed how to define a suitable connectivity function and integral transform for (1.1) posed on the Poincaré disc. Secondly, it is not clear how to define the Core and far-field manifolds in order to carry out the matching. In this paper, we show how this problem can be overcome. It turns out that the far-field manifold is easier to define than in the Euclidean case since there is no bifurcation in the far-field. At infinity, the splitting of the eigenvalues does not occur on the imaginary axis but on the axis $-\frac{1}{2} + \mathrm{i}\mathbb{R}$ and creates a stable fast and slow manifolds. We show, by requiring finite energy, that it is possible to find an intersection of the fast stable manifold and the Core manifold. On the other hand, calculating the Core manifold is significantly more involved than in the Euclidean case and constitutes the main challenge in the existence proof of spots in hyperbolic geometry. In fact, the Core manifold is found by carrying out an asymptotic expansion involving associated Legendre functions of the first an second kind.

Along with the analytical study, we present a numerical investigation of different types of 2D fully localized solutions found on connected solution branches related to the spot states using the numerical continuation package AUTO07p [37]. Extensive novel numerical methods have been developed for the Swift–Hohenberg equation to carry out numerical continuation for fully localized 2D patterns in order to gain insight into the bifurcation structure away from onset; see [78]. We show how these methods can be applied to (1.1) and how stability can also be computed. We identify the exact regions of parameter space for which linearly stable localized solutions persist in terms of one parameter governing the shape of the nonlinearity and a second parameter governing the shape of the connectivity function. Furthermore, we

investigate non-radially symmetric localized solutions that have symmetry properties particular to the specific geometry under study; in the Euclidean case $\boldsymbol{D}_6$-symmetric solutions and in the hyperbolic case $\boldsymbol{D}_8$-symmetric solutions.

This paper is divided into three parts. The first part is dedicated to the presentation of the models and the statement of the main theorems in section 2.1 and section 2.2. The second part, section 3, is devoted to the theoretical analysis of our models and the proofs of our theorems. We apply techniques from Scheel [90] and Lloyd and Sandstede [77] to prove the existence of a bifurcated branch of spot (Spot A) solutions near a Turing instability for the Euclidean case and extend our results to the hyperbolic case. In the last part, section 4, we use numerical continuation in order to extend the study by path following the solutions found in the analytical studies; we identify in terms of two parameters the regions of parameter space for which stable, radially symmetric, localized solutions exist. Furthermore, we find and path follow connected branches of non-radially symmetric solutions. Finally, in section 5 we conclude with a discussion of the relevance of the localized states found to the study of neural field models and associated applications.

## 2. The neural field models and main results

### *2.1. Neural field model of short term memory on the Euclidean plane*

The time evolution of the average membrane potential $v(\boldsymbol{r}, t)$ at time $t$ and position $\boldsymbol{r}$ in the visual cortex, abstracted by $\mathbb{R}^2$, is modelled by the following Wilson–Cowan neural field equation [1, 40, 41, 93]

$$\partial_t v(\boldsymbol{r}, t) = -v(\boldsymbol{r}, t) + \int_{\mathbb{R}^2} W(\|\boldsymbol{r} - \boldsymbol{r}'\|) S(\mu v(\boldsymbol{r}', t))\, \mathrm{d}\boldsymbol{r}', \tag{2.1}$$

where $\|\cdot\|$ is the standard Euclidean norm. The nonlinear firing rate function $S$ is defined by

$$S(x) = \frac{1}{1 + \mathrm{e}^{-x+\theta}} - \frac{1}{1 + \mathrm{e}^{\theta}}. \tag{2.2}$$

$\theta$ is a positive threshold and the parameter $\mu$ in (2.1) describes the stiffness of the sigmoid $S$. The connectivity function $W$ expresses interactions between populations of neurons located at position $\boldsymbol{r}$ and $\boldsymbol{r}'$ in the visual cortex and is defined through its *Hankel transform* in the following way

$$W(x) = \int_0^{+\infty} s\widehat{W}(s) J_0(xs)\, \mathrm{d}s, \qquad \widehat{W}(s) = 2\left(\frac{b_1\sigma_1}{\sigma_1^2 + s^2} - \frac{b_2\sigma_2}{\sigma_2^2 + s^2}\right). \tag{2.3}$$

$J_0(s)$ is the Bessel function of first kind and $(b_1, b_2, \sigma_1, \sigma_2)$ are real parameters. $\widehat{W}(\|\boldsymbol{k}\|)$ is the Fourier transform of $W(\|\boldsymbol{r}\|)$ for all $(\boldsymbol{r}, \boldsymbol{k}) \in \mathbb{R}^2$. One of the major modelling issues is to determine how localized solutions of equation (2.1) depend on the connectivity function $W$. Here we assume the connectivity function $W$ has a 'Mexican hat' shape. This type of connectivity function can be regarded as a two-layer model in which the inhibition is linear and very fast; see [86, 87]. The parameters $(b_1, b_2, \sigma_1, \sigma_2)$ are chosen such that hypothesis 2.1 is satisfied.

**Hypothesis 2.1.** *We assume that the connectivity function $W(x)$ and its corresponding Fourier transform $\widehat{W}(\|\boldsymbol{k}\|)$ satisfy the following conditions:*

*(i)* $\widehat{W}(0) = \widehat{W}_0 < 0$,
*(ii)* $W(0) > 0$,
*(iii) there exists* $k_c > 0$ *such that* $\widehat{W}_c \overset{\text{def}}{=} \widehat{W}(k_c) = \max_{k=\|\boldsymbol{k}\| \in \mathbb{R}^+} \widehat{W}(k) > 0$.

*For mathematical simplicity, we further assume that* $k_c = 1$ *throughout the paper.*

We define

$$\begin{aligned}\Gamma_1 &= 2\sigma_1\sigma_2(b_1\sigma_2 - b_2\sigma_1),\\ \Gamma_2 &= 2(b_1\sigma_1 - b_2\sigma_2),\end{aligned} \tag{2.4}$$

such that $\widehat{W}_c$ can be written

$$\widehat{W}_c = \frac{\Gamma_1 + \Gamma_2}{1 + \sigma_1^2 + \sigma_2^2 + \sigma_1^2\sigma_2^2}. \tag{2.5}$$

The condition $k_c = 1$, which is equivalent to $(\mathrm{d}/\mathrm{d}s)\widehat{W}(s)|_{s=1} = 0$, reduces to

$$\Gamma_1(\sigma_1^2 + \sigma_2^2 + 2) + \Gamma_2(1 - \sigma_1^2\sigma_2^2) = 0. \tag{2.6}$$

It is a straightforward computation to see that equations (2.5) and (2.6) imply that

$$\begin{aligned}\sigma_1^2\sigma_2^2 - \Gamma_1\widehat{W}_c^{-1} &= 1,\\ \sigma_1^2 + \sigma_2^2 - \Gamma_2\widehat{W}_c^{-1} &= -2.\end{aligned} \tag{2.7}$$

We define for all $k \geqslant 1$, $s_k = S^{(k)}(0)$, the $k$th derivative of $S$ evaluated at zero.

**Remark 2.1.** The dependence, with respect to the connectivity function, of the existence of stationary localized solutions of equation (2.1) in the case where the visual cortex is further approximated by $\mathbb{R}$ has been discussed in [46].

We can now state the first of our two theorems.

**Theorem 2.1 (Existence of spot solutions in Euclidean geometry).** *Fix* $\theta \geqslant 0$ *for the threshold of the nonlinearity* $S$ *and* $(b_1, b_2, \sigma_1, \sigma_2) \in \mathbb{R}^4$ *such that the connectivity function* $W$ *defined in equation (2.3) satisfies hypotheses 2.1. Then there exists* $\mu_* < \mu_c = (s_1\widehat{W}_c)^{-1}$ *such that the planar neural field equation (2.1) has a stationary localized radial solution* $v(r) \in L^2(\mathbb{R}^+, r\mathrm{d}r)$[5] *for each* $\mu \in ]\mu_*, \mu_c[$*: these solutions stay close to* $v = 0$ *and, for each fixed* $r_* > 0$*, we have the asymptotics*

$$v(r) = \alpha\sqrt{\mu_c - \mu}J_0(r) + O(\mu - \mu_c) \qquad \text{as } \mu \to \mu_c, \tag{2.8}$$

*uniformly in* $0 \leqslant r \leqslant r_*$ *for an appropriate constant* $\alpha$ *with* $\mathrm{sign}(\alpha) = \mathrm{sign}(s_2)$.

### *2.2. Neural field model of edges and textures selectivity on the Poincaré disc*

The selectivity of the responses of individual neurons to external features are often the basis of neuronal representations of the external world. For example, neurons in the primary visual cortex '(V1)' respond preferentially to visual stimuli that have a specific orientation [14, 18, 58], spatial frequency [16], velocity, direction of motion [84], and color [59]. A local network in the primary visual cortex, roughly 1 mm$^2$ of cortical surface, is assumed to consist of neurons coding for a given position in the retina for a full functional set of orientations and ocular dominance (the tendency to prefer visual input from one eye to the other). These subgroups are the so-called Hubel and Wiesel hypercolumns of V1 [60]. A new approach to model the processing of image edges and textures in the hypercolumns of area V1 based on a nonlinear representation of the image first order derivatives called the structure tensor [15, 70] was introduced in [26, 48]. It was suggested that this structure tensor was represented by neuronal populations in the hypercolumns of V1 and that the time evolution of this representation was governed by equations similar to those proposed by Wilson and Cowan [99, 100]. Structure

[5] $L^2(\mathbb{R}^+, r\mathrm{d}r) = \{v : \mathbb{R}^+ \to \mathbb{R} \mid \left(\int_0^{+\infty} v(r)^2 r\mathrm{d}r\right)^{1/2} < \infty\}$.

tensors are essentially $2 \times 2$ symmetric, positive definite matrices. The set of structure tensors therefore forms a solid open cone in $\mathbb{R}^3$, which is a Riemannian manifold foliated by hyperbolic planes. By a suitable change of coordinates, the hyperbolic plane can be further identified with the Poincaré disc $\mathbb{D} = \{z \in \mathbb{C} \mid |z| < 1\}$. Therefore, there is an isomorphism between the space of structure tensors and the product space $(0, +\infty[ \times \mathbb{D}$, on which the distance between points $(\delta, z)$ and $(\delta', z')$ is given by

$$d(\delta, z; \delta', z') = \sqrt{\log^2\left(\frac{\delta}{\delta'}\right) + d_{\mathbb{D}}(z, z')^2}, \tag{2.9}$$

where the second term under the radical is the usual 'hyperbolic' distance in $\mathbb{D}$:

$$d_{\mathbb{D}}(z, z') = 2\,\operatorname{atanh}\left(\frac{|z - z'|}{|1 - \bar{z}z'|}\right). \tag{2.10}$$

As shown in [27], we are able to neglect the dependence on $\delta \in \mathbb{R}_*^+ = (0, +\infty[$ as it does not play a significant role in the analysis that follows. Hence, we can consider the following neural field equation, set on the Poincaré disc, for the average membrane potential within such a hypercolumn

$$\partial_t v(z, t) = -v(z, t) + \int_{\mathbb{D}} W(d_{\mathbb{D}}(z, z'))S(\mu v(z', t))\mathrm{dm}(z'). \tag{2.11}$$

The measure element $\mathrm{dm}(\cdot)$ is given by the formula:

$$\mathrm{dm}(z) = \frac{4\mathrm{d}z\mathrm{d}\bar{z}}{(1 - |z|^2)^2}. \tag{2.12}$$

The nonlinearity $S$ has already been defined in equation (2.2). We work in geodesic polar coordinates $z = (\tau, \varphi) \in \mathbb{D}$, with $z = \tanh(\tau/2)\mathrm{e}^{\mathrm{i}\varphi}$. In this coordinate system, the measure element defined in equation (2.12) is transformed into $\mathrm{dm}(z) = \sinh(\tau)\,\mathrm{d}\tau\mathrm{d}\varphi$. As we want to prove the existence of radial solutions ($\tau$ being the radial coordinate), we define the equivalent of the Hankel transform for the hyperbolic disc, the *Mehler–Fock transform*, and we adopt the notations defined in [54].

**Definition 2.1.** *We denote by $\mathcal{P}_\nu^\mu(z)$ and $\mathcal{Q}_\nu^\mu(z)$ the two associated Legendre function of first kind and second kind, respectively, solutions of the equation*

$$(1 - z^2)\frac{\mathrm{d}^2}{\mathrm{d}z^2}u(z) - 2z\frac{\mathrm{d}}{\mathrm{d}z}u(z) + \left(\nu(\nu + 1) - \frac{\mu^2}{1 - z^2}\right)u(z) = 0. \tag{2.13}$$

Let $f : \mathbb{R}_*^+ \to \mathbb{R}$ be such that $f(\tau)\mathrm{e}^{\tau/2} \in \mathrm{L}^1(\mathbb{R}_*^+)$, then we define for all $\rho > 0$ and all $\tau > 0$ the Mehler–Fock transform of $f$ as

$$\mathcal{M}f(\rho) = \int_0^{+\infty} f(\tau)\mathcal{P}_{-\frac{1}{2}+\mathrm{i}\rho}(\cosh\tau)\sinh\tau\,\mathrm{d}\tau, \tag{2.14}$$

where we used the convention that $\mathcal{P}_\nu = \mathcal{P}_\nu^0$. The inversion formula states that

$$f(\tau) = \int_0^{+\infty} \mathcal{M}f(\rho)\mathcal{P}_{-\frac{1}{2}+\mathrm{i}\rho}(\cosh\tau)\rho\tanh(\pi\rho)\,\mathrm{d}\rho. \tag{2.15}$$

Moreover, we denote $L_{\mathbb{D}}^\tau$ to be the radial part of the Laplace–Beltrami operator on $\mathbb{D}$ defined by

$$L_{\mathbb{D}}^\tau = \frac{1}{\sinh\tau}\frac{d}{\mathrm{d}\tau}\left(\sinh\tau\frac{d}{\mathrm{d}\tau}\right). \tag{2.16}$$

It was shown in [54] that for all $k \geqslant 1$

$$(-1)^k \left(\frac{1}{4}+\rho^2\right)^k \mathcal{M}f(\rho) = \int_0^{+\infty} \left(L_{\mathbb{D}}^{\tau}\right)^k f(\tau)\mathcal{P}_{-\frac{1}{2}+\mathrm{i}\rho}(\cosh\tau)\sinh\tau\,\mathrm{d}\tau,$$

$$(-1)^k \left(L_{\mathbb{D}}^{\tau}\right)^k f(\tau) = \int_0^{+\infty} \left(\frac{1}{4}+\rho^2\right)^k \mathcal{M}f(\rho)\mathcal{P}_{-\frac{1}{2}+\mathrm{i}\rho}(\cosh\tau)\rho\tanh(\pi\rho)\,\mathrm{d}\rho. \tag{2.17}$$

Furthermore, for $\Re a > 0$ the following formula holds (Gradshteyn and Ryzhik 7.213 [55]):

$$\int_0^{+\infty} \frac{1}{a^2+\rho^2}\mathcal{P}_{-\frac{1}{2}+\mathrm{i}\rho}(\cosh\tau)\rho\tanh(\pi\rho)\,\mathrm{d}\rho = \mathcal{Q}_{a-\frac{1}{2}}(\cosh\tau),$$

where $\mathcal{Q}_\nu$ is the associated Legendre function of the second kind. From equations (2.14) and (2.15), we find that

$$\frac{1}{a^2+\rho^2} = \int_0^{+\infty} \mathcal{Q}_{a-\frac{1}{2}}(\cosh\tau)\mathcal{P}_{-\frac{1}{2}+\mathrm{i}\rho}(\cosh\tau)\sinh\tau\,\mathrm{d}\tau. \tag{2.18}$$

A computationally convenient choice for the connectivity function $W$ is then:

$$\boldsymbol{W}(z) = W(d_{\mathbb{D}}(z,0)) = \alpha_1\mathcal{Q}_{a_1-\frac{1}{2}}(\cosh d_{\mathbb{D}}(z,0)) - \alpha_2\mathcal{Q}_{a_2-\frac{1}{2}}(\cosh d_{\mathbb{D}}(z,0)), \tag{2.19}$$

with $(\alpha_1, \alpha_2, a_1, a_2)$ satisfying the relations

$$\begin{aligned} \alpha_1 &= 2\sigma_1 b_1, \\ \alpha_2 &= 2\sigma_2 b_2, \\ a_1 &= \sqrt{\sigma_1^2+\tfrac{1}{4}}, \\ a_2 &= \sqrt{\sigma_2^2+\tfrac{1}{4}}. \end{aligned} \tag{2.20}$$

From equation (2.18) and the definition of the Mehler–Fock transform, we have that for all $\rho > 0$

$$\widetilde{W}(\rho) \overset{\text{def}}{=} \mathcal{M}\boldsymbol{W}(\rho) = 2\left(\frac{b_1\sigma_1}{\sigma_1^2+\frac{1}{4}+\rho^2} - \frac{b_2\sigma_2}{\sigma_2^2+\frac{1}{4}+\rho^2}\right). \tag{2.21}$$

Comparing (2.21) with (2.3), we see that the transformed connectivity functions are equivalent.

As in the first section, we impose some conditions on the coefficients $(b_1, b_2, \sigma_1, \sigma_2)$ and assume $W$ satisfies hypothesis 2.2

**Hypothesis 2.2.** *We assume that the connectivity function $W$ and its corresponding Mehler–Fock transform $\widetilde{W}(\rho)$ ($\widetilde{\cdot}$ denotes Mehler–Fock transform) satisfy the following conditions:*

*(i)* $\widetilde{W}(0) = \widetilde{W}_0 < 0$,
*(ii)* $W(0) > 0$,
*(iii) there exists* $\rho_c > 0$ *such that* $\widetilde{W}_c \overset{\text{def}}{=} \widetilde{W}(\rho_c) = \max_{\rho\in\mathbb{R}^+} \widetilde{W}(\rho) > 0$.

*For mathematical simplicity, we further assume that* $\rho_c = \frac{\sqrt{3}}{2}$ *throughout the paper.*

Using the constants $\Gamma_1$ and $\Gamma_2$ defined in equation (2.4), $\widetilde{W}_c$ can be written as

$$\widetilde{W}_c = \frac{\Gamma_1+\Gamma_2}{1+\sigma_1^2+\sigma_2^2+\sigma_1^2\sigma_2^2}. \tag{2.22}$$

The condition $\rho_c = \sqrt{3}/2$, which is equivalent to $(\mathrm{d}/\mathrm{d}\rho)\widetilde{W}(\rho)|_{\rho=\sqrt{3}/2} = 0$, reduces to equation (2.6). It is also straightforward to see that equations (2.22) and (2.6) imply the relation given in equation (2.7).

We can now state the main result of the paper.

**Theorem 2.2 (Existence of spot solutions in hyperbolic geometry).** *Fix $\theta \geqslant 0$ for the threshold of the nonlinearity $S$ and $(b_1, b_2, \sigma_1, \sigma_2) \in \mathbb{R}^4$ such that the connectivity function $W$ defined in equation (2.19) satisfies hypotheses 2.2. Then there exists $\mu_* < \mu_c = (s_1 \widetilde{W}_c)^{-1}$ such that the planar neural field equation (2.11) has a stationary localized radial solution $v(\tau) \in L^2(\mathbb{R}^+, \sinh(\tau)\,\mathrm{d}\tau)$ for each $\mu \in ]\mu_*, \mu_c[$: these solutions stay close to $v = 0$ and, for each fixed $\tau_* > 0$, we have the asymptotics*

$$v(\tau) = \beta\sqrt{\mu_c - \mu}\,\mathcal{P}_{-\frac{1}{2}+\mathrm{i}\frac{\sqrt{3}}{2}}(\cosh\tau) + O(\mu - \mu_c) \qquad \text{as } \mu \to \mu_c, \tag{2.23}$$

*uniformly in $0 \leqslant \tau \leqslant \tau_*$ for an appropriate constant $\beta$ with $\operatorname{sign}(\beta) = -\operatorname{sign}(\Xi_{\tilde{d}_1^2})$, where*

$$\Xi_{\tilde{d}_1^2} = \frac{\mu_c^2 s_2}{2}\Bigg( -(\Gamma_1 + 2\Gamma_2)\int_0^\infty (\mathcal{P}_\nu(\cosh(s)))^3 \sinh(s)\,\mathrm{d}s + 2\Gamma_2 \times \int_0^\infty \mathcal{P}_\nu(\cosh(s))(\mathcal{P}_\nu^1(\cosh(s)))^2 \sinh(s)\,\mathrm{d}s + o(1)\Bigg).$$

**Remark 2.2.** The matching arguments in section 3 yield a similar theorem for the case $\mu > \mu_c$ where one finds a bifurcating branch of solutions also given by (2.23). However, these solutions are not $L^2(\mathbb{R}^+, \sinh(\tau)\,\mathrm{d}\tau)$-functions.

## 3. Radial analysis

### *3.1. Localized radial solutions in Euclidean geometry*

*3.1.1. Linear stability analysis of the trivial state.* Linearising equation (2.1) about the trivial equilibrium $v = 0$ yields the equation

$$\partial_t u(\boldsymbol{r}, t) = -u(\boldsymbol{r}, t) + \mu s_1 \int_{\mathbb{R}^2} W(\|\boldsymbol{r} - \boldsymbol{r}'\|)u(\boldsymbol{r}', t)\,\mathrm{d}\boldsymbol{r}'. \tag{3.1}$$

Looking for a Turing instability we set $u(\boldsymbol{r}, t) = \mathrm{e}^{\sigma t}\mathrm{e}^{\mathrm{i}\boldsymbol{k}\cdot\boldsymbol{r}}$ to obtain the dispersion relation

$$\sigma(\|\boldsymbol{k}\|) = -1 + \mu s_1 \widehat{W}(\|\boldsymbol{k}\|). \tag{3.2}$$

The critical value $\mu_c$ is then found to be given by

$$\mu_c = \frac{1}{s_1 \widehat{W}_c}, \tag{3.3}$$

and for all $\mu < \mu_c$, the trivial solution $v = 0$ is stable. Hence, we set $\lambda = \mu - \mu_c$ and rewrite equation (2.1) as

$$\partial_t v(\boldsymbol{r}, t) = \boldsymbol{L}_{\mu_c} v(\boldsymbol{r}, t) + \boldsymbol{R}(v(\boldsymbol{r}, t), \lambda), \tag{3.4}$$

where $\boldsymbol{L}_{\mu_c}$ and $\boldsymbol{R}$ are defined by

$$\begin{aligned} \boldsymbol{L}_{\mu_c} v(\boldsymbol{r}, t) &= -v(\boldsymbol{r}, t) + \mu_c s_1 \int_{\mathbb{R}^2} W(\|\boldsymbol{r} - \boldsymbol{r}'\|)v(\boldsymbol{r}', t)\,\mathrm{d}\boldsymbol{r}', \\ \boldsymbol{R}(v(\boldsymbol{r}, t), \lambda) &= \int_{\mathbb{R}^2} W(\|\boldsymbol{r} - \boldsymbol{r}'\|)\left[S\left((\lambda + \mu_c)v(\boldsymbol{r}', t)\right) - \mu_c s_1 v(\boldsymbol{r}', t)\right]\mathrm{d}\boldsymbol{r}'. \end{aligned}$$

Note that $\boldsymbol{R}(0, 0) = D_v\boldsymbol{R}(0, 0) = 0$. In general, we define $f(X, \lambda)$ by

$$f(X, \lambda) = S\left((\lambda + \mu_c)X\right) - \mu_c s_1 X,$$

where, by construction, $f(0, 0) = \partial_X f(0, 0) = 0$.

*3.1.2. PDE method* We assume that $v \to v(\cdot,t) \in \mathcal{C}^1(\mathbb{R}^+, \mathcal{H}^4(\mathbb{R}^2))$ is a solution of (3.4), where $\mathcal{H}^4(\mathbb{R}^2)$ is the Sobolev space defined as

$$\mathcal{H}^4(\mathbb{R}^2) = \{u \in \mathrm{L}^2(\mathbb{R}^2) \mid \forall\, 0 \leqslant |\alpha| \leqslant 4\ D^\alpha u \in \mathrm{L}^2(\mathbb{R}^2)\}.$$

Under this assumption, an application of the Fourier transform to equation (3.4) yields

$$(\partial_t + 1)\,\widehat{v}(\boldsymbol{k},t) = \widehat{W}(\|\boldsymbol{k}\|)\left[\mu_c s_1 \widehat{v}(\boldsymbol{k},t) + \widehat{f(v,\lambda)}(\boldsymbol{k},t)\right].$$

Using the inverse Fourier transform we then obtain

$$(\partial_t + 1)\,\mathcal{L}_{\mu_c}(v) = \mathcal{M}(v,\lambda), \tag{3.5}$$

with $\mathcal{L}_{\mu_c}$ and $\mathcal{M}$ defined by

$$\mathcal{L}_{\mu_c}(v) = (\sigma_1^2\sigma_2^2 - \Gamma_1\mu_c s_1)v - (\sigma_1^2 + \sigma_2^2 - \Gamma_2\mu_c s_1)\Delta v + \Delta^2 v,$$

and

$$\mathcal{M}(v,\lambda) = \Gamma_1 f(v,\lambda) - \Gamma_2 \Delta f(v,\lambda),$$

where $\Delta$ denotes the Laplacian on $\mathbb{R}^2$. From equations (2.7) and the fact that $\mu_c = \left(s_1 \widehat{W}_c\right)^{-1}$, the coefficients of $\mathcal{L}_{\mu_c}$ reduce to

$$\begin{aligned} \sigma_1^2\sigma_2^2 - \Gamma_1\mu_c s_1 &= 1, \\ \sigma_1^2 + \sigma_2^2 - \Gamma_2\mu_c s_1 &= -2. \end{aligned}$$

We look for stationary radial solutions of equation (3.4), that is

$$v(r) + 2\Delta_r v(r) + \Delta_r^2 v(r) = \Gamma_1 f(v(r),\lambda) - \Gamma_2 \Delta_r f(v(r),\lambda) \tag{3.6}$$

with $r = \|\boldsymbol{r}\| \in \mathbb{R}^+$ and $\Delta_r = \partial_r^2 + (1/r)\partial_r$. Note that $\Delta_r f(v(r),\lambda)$ can be expressed as

$$\Delta_r f(v,\lambda) = (\Delta_r v)\, f'(v,\lambda) + (\partial_r v)^2\, f''(v,\lambda).$$

*3.1.3. The equation near the core.* We rewrite equation (3.6) as a four-dimensional spatial dynamical system. To do this, we set

$$\begin{aligned} &\partial_r u_1 = u_3, \\ &\partial_r u_2 = u_4, \\ &\left(\partial_r^2 + \frac{1}{r}\partial_r + 1\right) u_1 = u_2, \\ &\left(\partial_r^2 + \frac{1}{r}\partial_r + 1\right) u_2 = \Gamma_1 f(u_1,\lambda) - \Gamma_2 \Delta_r f(u_1,\lambda), \end{aligned}$$

and we can write

$$\partial_r U = \mathcal{A}(r)U + \mathcal{F}(U,\lambda), \tag{3.7}$$

where $U = (u_1, u_2, u_3, u_4)^{\mathrm{T}}$,

$$\mathcal{A}(r) = \begin{pmatrix} 0 & 0 & 1 & 0 \\ 0 & 0 & 0 & 1 \\ -1 & 1 & -\frac{1}{r} & 0 \\ 0 & -1 & 0 & -\frac{1}{r} \end{pmatrix}, \quad \mathcal{F}(U,\lambda) = \begin{pmatrix} 0 \\ 0 \\ 0 \\ \mathcal{F}_4(u_1,u_2,u_3,u_4,\lambda) \end{pmatrix}$$

and

$$\mathcal{F}_4(u_1,u_2,u_3,u_4,\lambda) = \Gamma_1 f(u_1,\lambda) - \Gamma_2\left[(u_2-u_1)f'(u_1,\lambda) + u_3^2 f''(u_1,\lambda)\right].$$

We can now apply the theory developed in [77, 90]. First, we set $\lambda = 0$ and linearize (3.7) about $U = 0$ to get the linear system $\partial_r U = \mathcal{A}(r)U$ which has four linearly independent solutions

$$\begin{aligned}
V_1(r) &= \sqrt{2\pi}\,(J_0(r), 0, -J_1(r), 0)^{\mathrm{T}}\\
V_2(r) &= \sqrt{2\pi}\,(rJ_1(r), 2J_0(r), rJ_0(r), -2J_1(r))^{\mathrm{T}}\\
V_3(r) &= \sqrt{2\pi}\,(Y_0(r), 0, -Y_1(r), 0)^{\mathrm{T}}\\
V_4(r) &= \sqrt{2\pi}\,(rY_1(r), 2Y_0(r), rY_0(r), -2Y_1(r))^{\mathrm{T}}
\end{aligned}$$

where $J_k$ and $Y_k$ denote the $k$th Bessel functions of the first and second kind, respectively. Lemma 3.1 defines the centre-unstable 'core' manifold $\mathcal{W}^{\mathrm{cu}}_-$ that describes all radial solutions that remain bounded as $r \to 0$. We denote by $P^{\mathrm{cu}}_-(r_0)$ the projection onto the space spanned by $V_{1,2}(r_0)$ with null space given by the span of $V_{3,4}(r_0)$.

Throughout this paper, we shall use the Landau symbols $O(\cdots)$ and $O_{r_0}(\cdots)$ with their usual meaning: the difference between the two symbols is that the constants that bound $O(\cdots)$ can be chosen independently of $r_0$, while the constants that bound $O_{r_0}(\cdots)$ may depend on $r_0$.

**Lemma 3.1.** *Fix $r_0 > 0$, then there exist constants $\delta_0, \delta_1$ such that the set $\mathcal{W}^{\mathrm{cu}}_-(\lambda)$ of solutions $U(r)$ of (3.7) for which $\sup_{0\leqslant r\leqslant r_0}|U(r)| < \delta_0$ is, for $|\lambda| < \delta_0$, is a smooth two-dimensional manifold. Furthermore, $U \in \mathcal{W}^{\mathrm{cu}}_-(\lambda)$ with $|P^{\mathrm{cu}}_-(r_0)U(r_0)| < \delta_1$ if and only if*

$$\begin{aligned}
U(r_0) = {}& \tilde{d}_1 V_1(r_0) + \tilde{d}_2 V_2(r_0) + V_3(r_0) O_{r_0}(|\lambda||\tilde{d}| + |\tilde{d}|^2)\\
&+ V_4(r_0)\left(\Theta_{\tilde{d}_1^2}\tilde{d}_1^2 + \Theta_{\tilde{d}_1\tilde{d}_2}\tilde{d}_1\tilde{d}_2 + O_{r_0}(|\lambda||\tilde{d}| + |\tilde{d}_2|^2 + |\tilde{d}|^3)\right),
\end{aligned} \tag{3.8}$$

*where*

$$\begin{aligned}
\Theta_{\tilde{d}_1^2} &= \sqrt{2\pi}\,\mu_{\mathrm{c}}^2 s_2 \frac{\Gamma_1 + \Gamma_2}{4}\left[\frac{1}{\sqrt{3}} + O(r_0^{-1/2})\right],\\
\Theta_{\tilde{d}_1\tilde{d}_2} &= -\sqrt{2\pi}\,\mu_{\mathrm{c}}^2 s_2 \Gamma_2\left[\frac{1}{\sqrt{3}} + O(r_0^{-1/2})\right],
\end{aligned}$$

*for some $\tilde{d} = (\tilde{d}_1, \tilde{d}_2) \in \mathbb{R}^2$ with $|\tilde{d}| < \delta_1$, where the right-hand side in (3.8) depends smoothly on $(\tilde{d}, \lambda)$.*

**Proof.** We observe that four independent solutions to the adjoint problem $\partial_r U = -\mathcal{A}^{\mathrm{T}}(r)U$ are given by

$$\begin{aligned}
W_1(r) &= \frac{\sqrt{2\pi}}{8}\left(-2rY_1(r), r^2Y_0(r), -2rY_0(r), -r^2Y_1(r)\right)^{\mathrm{T}},\\
W_2(r) &= \frac{\sqrt{2\pi}}{8}\,(0, -rY_1(r), 0, -rY_0(r))^{\mathrm{T}},\\
W_3(r) &= \frac{\sqrt{2\pi}}{8}\left(2rJ_1(r), -r^2J_0(r), 2rJ_0(r), r^2J_1(r)\right)^{\mathrm{T}},\\
W_4(r) &= \frac{\sqrt{2\pi}}{8}\,(0, rJ_1(r), 0, rJ_0(r))^{\mathrm{T}}.
\end{aligned}$$

It follows from

$$\frac{\pi}{2} r\,(J_1(r)Y_0(r) - J_0(r)Y_1(r)) = 1,$$

that

$$\langle V_i(r), W_j(r)\rangle_{\mathbb{R}^4} = \delta_{i,j} \qquad i, j = 1, \ldots, 4,$$

is independent of $r$. For given $\tilde{d} = (\tilde{d}_1, \tilde{d}_2) \in \mathbb{R}^2$, we consider the fixed-point equation

$$\begin{aligned} U(r) &= \sum_{j=1}^{2} \tilde{d}_j V_j(r) + \sum_{j=1}^{2} V_j(r) \int_{r_0}^{r} \langle W_j(s), \mathcal{F}(U(s), \lambda) \rangle \, \mathrm{d}s \\ &\quad + \sum_{j=3}^{4} V_j(r) \int_{0}^{r} \langle W_j(s), \mathcal{F}(U(s), \lambda) \rangle \, \mathrm{d}s, \\ &= \sum_{j=1}^{2} \tilde{d}_j V_j(r) + \sum_{j=1}^{2} V_j(r) \int_{r_0}^{r} W_{j,4}(s) \mathcal{F}_4(U(s), \lambda) \, \mathrm{d}s \\ &\quad + \sum_{j=3}^{4} V_j(r) \int_{0}^{r} W_{j,4}(s) \mathcal{F}_4(U(s), \lambda) \, \mathrm{d}s \end{aligned} \tag{3.9}$$

on $\mathcal{C}^0([0, r_0], \mathbb{R}^4)$, where $W_{j,4}(r)$ (respectively $\mathcal{F}_4(U(r), \lambda)$)denotes the fourth component of $W_j(r)$ (respectively $\mathcal{F}(U(r), \lambda)$). A direct adaptation of lemma 1 in [77] gives

- Each solution $U \in \mathcal{C}^0([0, r_0], \mathbb{R}^4)$ of (3.9) gives a solution of (3.7) that is bounded on $[0, r_0]$.
- Every bounded solution $U \in \mathcal{C}^0([0, r_0], \mathbb{R}^4)$ of (3.7) satisfies (3.9) provided that we add $\tilde{d}_3 V_3(r) + \tilde{d}_4 V_4(r)$ to the right-hand side for an appropriate $\tilde{d} \in \mathbb{R}^4$.
- Existence of solutions of (3.9) is given by the uniform contraction mapping principle for sufficiently small $(\tilde{d}_1, \tilde{d}_2)$ and $\lambda$.
- The resulting solution $U$ satisfies on $[0, r_0]$

$$U(r) = \sum_{j=1}^{2} \tilde{d}_j V_j(r) + O_{r_0}(|\lambda||\tilde{d}| + |\tilde{d}|^2).$$

As in [77], we need to calculate the quadratic coefficient in $\tilde{d}$ in front of $V_4(r_0)$, denoted $\Theta$. The quadratic term in $U$ of $\mathcal{F}(U, \lambda)$ at $(0, 0)$ is given by

$$\mathcal{F}_{20}(U, U) = \frac{\mu_c^2 s_2}{2} \left(0, 0, 0, (\Gamma_1 + 2\Gamma_2)u_1^2 - 2\Gamma_2 u_1 u_2 - 2\Gamma_2 u_3^2\right)^{\mathrm{T}}.$$

If we evaluate (3.9) at $r = r_0$, we arrive at (3.8) except that we need to calculate the quadratic coefficients in front of $V_4(r_0)$. Using a Taylor expansion, we find that these coefficients are given by

$$\Theta_{\tilde{d}_1^2} = \int_0^{r_0} W_{4,4}(s) \pi \mu_c^2 s_2 \left[(\Gamma_1 + 2\Gamma_2) J_0(s)^2 - 2\Gamma_2 J_1(s)^2\right] \mathrm{d}s,$$

and

$$\Theta_{\tilde{d}_1 \tilde{d}_2} = -4 \int_0^{r_0} W_{4,4}(s) \pi \mu_c^2 s_2 \Gamma_2 J_0(s)^2 \, \mathrm{d}s.$$

Using the two formulas for integrals of Bessel functions

$$\begin{aligned} \int_0^{+\infty} J_\nu(as) J_\nu(bs) J_\nu(cs) s^{1-\nu} \, \mathrm{d}s &= \frac{2^{\nu-1} \triangle^{2\nu-1}}{(abc)^\nu \Gamma(\nu + \frac{1}{2}) \Gamma(\frac{1}{2})}, \\ \int_0^{+\infty} J_\mu(as) J_\nu(bs) J_\nu(cs) s^{1-\mu} \, \mathrm{d}s &= \frac{(bc)^{\mu-1} \sin(A)^{\mu-1/2}}{\sqrt{2\pi} a^\mu} \mathcal{P}^{\frac{1}{2}-\mu}_{\nu-\frac{1}{2}}(\cos(A)), \end{aligned}$$

where $\triangle$ is the area of triangle with lengths $a$, $b$ and $c$, $A = \arccos\left((b^2+c^2-a^2)/2bc\right)$ and $\mathcal{P}$ is the associated Legendre function (see [97]), we find with $a=b=c=1$ and $\nu=0$ (i.e. $\triangle = \frac{\sqrt{3}}{4}$ and $\Gamma(\frac{1}{2}) = \sqrt{\pi}$)

$$\int_0^{+\infty} sJ_0(s)^3\,\mathrm{d}s = \frac{2}{\pi\sqrt{3}},$$

and with $a=b=c=1$, $\mu=0$ and $\nu=1$ $\left(\text{i.e. } A=\frac{\pi}{3} \text{ and } \mathcal{P}^{\frac{1}{2}}_{\frac{1}{2}}(z) = \sqrt{(2/\pi)}(z/(1-z^2)^{\frac{1}{4}})\right)$

$$\int_0^{+\infty} sJ_0(s)J_1(s)^2\,\mathrm{d}s = \frac{1}{\pi\sqrt{3}}.$$

We also have the estimates (see [80])

$$\int_{r_0}^{+\infty} sJ_0(s)^3\,\mathrm{d}s = O(r_0^{-1/2}),$$

and

$$\int_{r_0}^{+\infty} sJ_0(s)J_1(s)^2\,\mathrm{d}s = O(r_0^{-1/2}).$$

Thus we have

$$\begin{aligned}\Theta_{\tilde{d}_1^2} &= \frac{\sqrt{2\pi}\pi\mu_c^2 s_2(\Gamma_1+2\Gamma_2)}{8}\int_0^{r_0} sJ_0(s)^3\,\mathrm{d}s - \frac{\sqrt{2\pi}\pi\mu_c^2 s_2\Gamma_2}{4}\int_0^{r_0} sJ_0(s)J_1(s)^2\,\mathrm{d}s\\ &= \frac{\sqrt{2\pi}\pi\mu_c^2 s_2(\Gamma_1+2\Gamma_2)}{8}\left(\frac{2}{\pi\sqrt{3}}+O(r_0^{-1/2})\right) - \frac{\sqrt{2\pi}\pi\mu_c^2 s_2\Gamma_2}{4}\left(\frac{1}{\pi\sqrt{3}}+O(r_0^{-1/2})\right)\\ &= \frac{\sqrt{2\pi}\mu_c^2 s_2(\Gamma_1+\Gamma_2)}{4}\left(\frac{1}{\sqrt{3}}+O(r_0^{-1/2})\right)\end{aligned}$$

and

$$\begin{aligned}\Theta_{\tilde{d}_1\tilde{d}_2} &= -\frac{\sqrt{2\pi}\pi\mu_c^2 s_2\Gamma_2}{2}\int_0^{r_0} sJ_0(s)^3\,\mathrm{d}s\\ &= -\sqrt{2\pi}\mu_c^2 s_2\Gamma_2\left(\frac{1}{\sqrt{3}}+O(r_0^{-1/2})\right).\end{aligned}$$

□

*3.1.4. The far-field equations.* We make the spatial dynamical system (3.7) autonomous by adding the equation $\partial_r\alpha = -\alpha^2$ where $\alpha = (1/r)$. The augmented system becomes

$$\frac{\mathrm{d}}{\mathrm{d}r}\begin{pmatrix}u_1\\u_2\\u_3\\u_4\\\alpha\end{pmatrix} = \begin{pmatrix}u_3\\u_4\\-u_1+u_2-\alpha u_3\\-u_2-\alpha u_4+\mathcal{F}_4(u_1,u_2,u_3,u_4,\lambda)\\-\alpha^2\end{pmatrix}. \tag{3.10}$$

We now carry out a series of near-identity coordinate transformations to put (3.10) into normal form. To do this, we define the normal form coordinates

$$U = \widetilde{A}\zeta_0 + \widetilde{B}\zeta_1 + \text{c.c.}, \qquad U = (u_1,u_2,u_3,u_4)^{\mathrm{T}},$$

or equivalently

$$\begin{pmatrix}\widetilde{A}\\\widetilde{B}\end{pmatrix} = \frac{1}{4}\begin{pmatrix}2u_1-\mathrm{i}(2u_3+u_4)\\-u_4-\mathrm{i}u_2\end{pmatrix},$$

where $\mathcal{A}(\infty)\zeta_0 = \mathrm{i}\zeta_0$ and $\mathcal{A}(\infty)\zeta_1 = \mathrm{i}\zeta_1 + \zeta_0$ with

$$\mathcal{A}(\infty) = \begin{pmatrix} 0 & 0 & 1 & 0 \\ 0 & 0 & 0 & 1 \\ -1 & 1 & 0 & 0 \\ 0 & -1 & 0 & 0 \end{pmatrix}, \quad \zeta_0 = \begin{pmatrix} 1 \\ 0 \\ \mathrm{i} \\ 0 \end{pmatrix}, \quad \zeta_1 = \begin{pmatrix} 0 \\ 2\mathrm{i} \\ 1 \\ -2 \end{pmatrix}.$$

In these coordinates, equation (3.10) becomes

$$\begin{aligned} \partial_r \widetilde{A} &= \left(\mathrm{i} - \frac{\alpha}{2}\right)\widetilde{A} + \widetilde{B} + \frac{\alpha}{2}\overline{\widetilde{A}} + O((|\lambda| + |\widetilde{A}| + |\widetilde{B}|)(|\widetilde{A}| + |\widetilde{B}|)), \\ \partial_r \widetilde{B} &= \left(\mathrm{i} - \frac{\alpha}{2}\right)\widetilde{B} - \frac{\alpha}{2}\overline{\widetilde{B}} + O((|\lambda| + |\widetilde{A}| + |\widetilde{B}|)(|\widetilde{A}| + |\widetilde{B}|)), \\ \partial_r \alpha &= -\alpha^2. \end{aligned} \tag{3.11}$$

**Lemma 3.2.** *Fix $0 < m < \infty$, then there exists a change of coordinates*

$$\begin{pmatrix} A \\ B \end{pmatrix} = \mathrm{e}^{\mathrm{i}\phi(r)}[I + \mathcal{T}(\alpha)]\begin{pmatrix} \widetilde{A} \\ \widetilde{B} \end{pmatrix} + O((|\lambda| + |\widetilde{A}| + |\widetilde{B}|)(|\widetilde{A}| + |\widetilde{B}|)), \tag{3.12}$$

*so that (3.11) becomes*

$$\begin{aligned} \partial_r A &= -\frac{\alpha}{2}A + B + \mathcal{R}_A(A, B, \alpha, \lambda), \\ \partial_r B &= -\frac{\alpha}{2}B + c_1^1 \lambda A + c_3^0 |A|^2 A + \mathcal{R}_B(A, B, \alpha, \lambda), \\ \partial_r \alpha &= -\alpha^2. \end{aligned} \tag{3.13}$$

*The constants $c_1^1$ and $c_3^0$ are given by*

$$c_1^1 = -\frac{s_1(\Gamma_1 + \Gamma_2)}{4} \tag{3.14}$$

*and*

$$c_3^0 = -\frac{\mu_c^3(\Gamma_1 + \Gamma_2)}{4}\left[\frac{s_3}{2} + \frac{\mu_c s_2^2(19\Gamma_1 + 4\Gamma_2)}{18}\right]. \tag{3.15}$$

*The coordinate change is polynomial in $(A, B, \alpha)$ and smooth in $\lambda$ and $\mathcal{T}(\alpha) = O(\alpha)$ is linear and upper triangular for each $\alpha$, while $\phi(r)$ satisfies*

$$\partial_r \phi(r) = 1 + O(|\lambda| + |\alpha|^3 + |A|^2), \quad \phi(0) = 0.$$

*The remainder terms are given by*

$$\begin{aligned} \mathcal{R}_A(A, B, \alpha, \lambda) = O\Bigg(&\sum_{j=0}^{2} |A^j B^{3-j}| + |\alpha|^3|A| + |\alpha|^2|B| + (|A| + |B|)^5 \\ &+ |\lambda||\alpha|^m(|A| + |B|)\Bigg), \\ \mathcal{R}_B(A, B, \alpha, \lambda) = O\Bigg(&\sum_{j=0}^{1} |A^j B^{3-j}| + |\alpha|^3|B| + |\lambda|(|\lambda| + |\alpha|^3 + |A|^2)|A| \\ &+ (|A| + |B|)^5 + |\lambda||\alpha|^m|B|\Bigg). \end{aligned}$$

**Proof.** See Scheel [90] for the change of variables. The coefficients $c_1^1$ and $c_3^0$ have been computed in [46]. □

We set $\lambda = -\epsilon, \epsilon > 0$ and $c_1^0 = -c_1^1$. We define

$$A = \sqrt{\epsilon}a, \qquad B = \epsilon b, \qquad r = \frac{\rho}{\sqrt{\epsilon}}, \tag{3.16}$$

for which (3.13) becomes

$$\begin{aligned} \partial_\rho a &= b - \frac{a}{2\rho} + \mathcal{R}_1(a, b, \rho, \epsilon), \\ \partial_\rho b &= -\frac{b}{2\rho} + c_1^0 a + c_3^0 |a|^2 a + \mathcal{R}_2(a, b, \rho, \epsilon), \end{aligned} \tag{3.17}$$

where

$$\begin{aligned} \mathcal{R}_1(a, b, \rho, \epsilon) &= \epsilon^{-1}\mathcal{R}_A(\sqrt{\epsilon}a, \epsilon b, \frac{\sqrt{\epsilon}}{\rho}, \epsilon) = O(\epsilon(|a| + |b|)), \\ \mathcal{R}_2(a, b, \rho, \epsilon) &= \epsilon^{-3/2}\mathcal{R}_B(\sqrt{\epsilon}a, \epsilon b, \frac{\sqrt{\epsilon}}{\rho}, \epsilon) = O(\epsilon(|a| + |b|)), \end{aligned} \tag{3.18}$$

uniformly in $\rho \geqslant \rho_1$ for each fixed $\rho_1 > 0$. We also use the variables

$$\begin{pmatrix} a \\ b \end{pmatrix} = \frac{1}{\sqrt{\rho}} \begin{pmatrix} \hat{a} \\ \hat{b} \end{pmatrix}, \tag{3.19}$$

in which (3.17) becomes

$$\begin{aligned} \partial_\rho \hat{a} &= \hat{b} + O_\rho(\epsilon(|\hat{a}| + |\hat{b}|)), \\ \partial_\rho \hat{b} &= c_1^0 \hat{a} + \frac{c_3^0}{\rho}|\hat{a}|^2 \hat{a} + O_\rho(\epsilon(|\hat{a}| + |\hat{b}|)). \end{aligned} \tag{3.20}$$

The estimates for the remainder terms given above are valid for $\rho \geqslant \rho_1$ for each fixed $\rho_1 > 0$. To capture the region $r_0\sqrt{\epsilon} \leqslant \rho \leqslant \rho_1$, we use the variables

$$\begin{pmatrix} \tilde{a} \\ \tilde{b} \end{pmatrix} = \begin{pmatrix} a \\ \rho(b - \frac{a}{2\rho}) \end{pmatrix}, \quad \tau = \log \rho, \tag{3.21}$$

so that $\rho = e^\tau$ and $\rho \to 0$ corresponds to $\tau \to -\infty$. In these variables, (3.20) becomes

$$\begin{aligned} \partial_\tau \tilde{a} &= \tilde{b} + \tilde{\mathcal{R}}_1(\tilde{a}, \tilde{b}, \rho, \epsilon), \\ \partial_\tau \tilde{b} &= \frac{\tilde{a}}{4} + \rho^2 \left(c_1^0 \tilde{a} + c_3^0 |\tilde{a}|^2 \tilde{a}\right) + \tilde{\mathcal{R}}_2(\tilde{a}, \tilde{b}, \rho, \epsilon), \\ \partial_\tau \rho &= \rho, \end{aligned} \tag{3.22}$$

with $(\tilde{a}, \tilde{b}, \rho) \in \mathbb{C}^2 \times \mathbb{R}^+$.

*3.1.5. Matching the core and the far-field.* We start by linearizing the far-field equation (3.20) about $(\hat{a}, \hat{b}) = 0$ to get the equation

$$\partial_\rho \begin{pmatrix} \hat{a} \\ \hat{b} \end{pmatrix} = \begin{pmatrix} 0 & 1 \\ c_1^0 & 0 \end{pmatrix} \begin{pmatrix} \hat{a} \\ \hat{b} \end{pmatrix} + O(\epsilon) \begin{pmatrix} \hat{a} \\ \hat{b} \end{pmatrix}. \tag{3.23}$$

For $\epsilon = 0$, the general solution of (3.23) is given by

$$\begin{pmatrix} \hat{a} \\ \hat{b} \end{pmatrix}(\rho) = q_1 \mathrm{e}^{-\rho\sqrt{c_1^0}} \begin{pmatrix} 1 \\ -\sqrt{c_1^0} \end{pmatrix} + q_2 \mathrm{e}^{\rho\sqrt{c_1^0}} \begin{pmatrix} 1 \\ \sqrt{c_1^0} \end{pmatrix}.$$

Thus, for each $\rho = \rho_1 > 0$ and for sufficiently small $\epsilon > 0$, we can write the $\rho = \rho_1$-fiber of the stable manifold $\mathcal{W}^s_+(\epsilon)$ of (3.20) near 0 as

$$\mathcal{W}^s_+(\epsilon)\mid_{\rho=\rho_1} \; : \; \begin{pmatrix} \hat{a} \\ \hat{b} \end{pmatrix} = \eta \begin{pmatrix} 1 \\ -\sqrt{c_1^0} \end{pmatrix} + O_{\rho_1}(\epsilon|\eta| + |\eta|^3) \begin{pmatrix} 1 \\ \sqrt{c_1^0} \end{pmatrix},$$

where $\eta \in \mathbb{C}$. Using (3.19) and (3.21) and redefining $\eta$, we obtain the expression

$$\mathcal{W}^s_+(\epsilon)\mid_{\rho=\rho_1} \; : \; \begin{pmatrix} \tilde{a} \\ \tilde{b} \end{pmatrix} = \eta \begin{pmatrix} 1 \\ -\frac{1}{2} - \rho_1\sqrt{c_1^0} \end{pmatrix} + O_{\rho_1}(\epsilon|\eta| + |\eta|^3) \begin{pmatrix} 1 \\ -\frac{1}{2} + \rho_1\sqrt{c_1^0} \end{pmatrix},$$

for $\mathcal{W}^s_+(\epsilon)$ in the $(\tilde{a}, \tilde{b})$-coordinates. We introduce the coordinates

$$u = \begin{pmatrix} u_1 \\ u_2 \end{pmatrix} = \frac{1}{2}\begin{pmatrix} 1 & 2 \\ 1 & -2 \end{pmatrix}\begin{pmatrix} \tilde{a} \\ \tilde{b} \end{pmatrix}, \tag{3.24}$$

which yields

$$\mathcal{W}^s_+(\epsilon)\mid_{\rho=\rho_1} \; : \; \begin{pmatrix} u_1 \\ u_2 \end{pmatrix} = \eta \begin{pmatrix} -\rho_1\sqrt{c_1^0} \\ 1 + \rho_1\sqrt{c_1^0} \end{pmatrix} + O_{\rho_1}(\epsilon|\eta| + |\eta|^3) \begin{pmatrix} \rho_1\sqrt{c_1^0} \\ 1 - \rho_1\sqrt{c_1^0} \end{pmatrix}.$$

The $(u_1, u_2)$-coordinates transform equation (3.22) into

$$\partial_\tau u = \left[D + O(\epsilon \mathrm{e}^{-2\tau})\right] u + O((\sqrt{\epsilon} + e^\tau)e^\tau|u|), \quad D = \begin{pmatrix} \frac{1}{2} & 0 \\ 0 & -\frac{1}{2} \end{pmatrix}. \tag{3.25}$$

**Lemma 3.3.** *The linear equation*

$$\partial_\tau u = \left[D + O(\epsilon \mathrm{e}^{-2\tau})\right] u \tag{3.26}$$

*has an exponential dichotomy with exponents* $\pm\frac{1}{2}$ *on* $[\tau_0, \tau_1]$. *Furthermore, the coordinate transformation* $u \to \tilde{u}$ *that brings (3.26) into the form*

$$\partial_\tau \tilde{u} = \left[D + O(\epsilon \mathrm{e}^{-2\tau})Id\right] \tilde{u}, \tag{3.27}$$

*can be chosen such that*

$$u(\tau_0) = \tilde{u}(\tau_0), \quad u(\tau_1) = \begin{pmatrix} 1 & O(\epsilon) \\ O(r_0^{-2}) & 1 \end{pmatrix} \tilde{u}(\tau_1). \tag{3.28}$$

**Proof.** See [77]. □

We recall that we have

$$\mathcal{W}^s_+(\epsilon)\mid_{\rho=\rho_1} \; : \; \begin{pmatrix} u_1 \\ u_2 \end{pmatrix} = \eta \begin{pmatrix} -\rho_1\sqrt{c_1^0} \\ 1 + \rho_1\sqrt{c_1^0} \end{pmatrix} + O_{\rho_1}(\epsilon|\eta| + |\eta|^3) \begin{pmatrix} \rho_1\sqrt{c_1^0} \\ 1 - \rho_1\sqrt{c_1^0} \end{pmatrix}.$$

for the stable manifold in the $u$-variables, which thanks to (3.28), becomes

$$\begin{aligned} \mathcal{W}^s_+(\epsilon)\mid_{\rho=\rho_1} \; : \; \begin{pmatrix} \tilde{u}_1 \\ \tilde{u}_2 \end{pmatrix} &= \eta \begin{pmatrix} -\rho_1\sqrt{c_1^0} + O_{\rho_1}(\epsilon) \\ 1 + \rho_1\sqrt{c_1^0}(1 + O(r_0^{-2})) \end{pmatrix} \\ &\quad + O_{\rho_1}(\epsilon|\eta| + |\eta|^3) \begin{pmatrix} \rho_1\sqrt{c_1^0} + O_{\rho_1}(\epsilon) \\ 1 - \rho_1\sqrt{c_1^0}(1 + O(r_0^{-2})) \end{pmatrix}, \end{aligned}$$

in the $\tilde{u}$-variables. Choosing $0 < \rho_1 \ll 1$ sufficiently small, we can solve

$$\eta\left(1+\rho_1\sqrt{c_1^0}(1+O(r_0^{-2}))\right)+O_{\rho_1}(\epsilon|\eta|+|\eta|^3)\left(1-\rho_1\sqrt{c_1^0}(1+O(r_0^{-2}))\right)=\tilde{\eta},$$

for $\eta$ so that

$$\eta=\frac{\tilde{\eta}}{1+\rho_1\sqrt{c_1^0}\left(1+O(r_0^{-2})\right)}+O_{\rho_1}(\epsilon|\tilde{\eta}|+|\tilde{\eta}|^3),$$

and consequently

$$\mathcal{W}_+^s(\epsilon)\mid_{\rho=\rho_1}\ :\ \begin{pmatrix}\tilde{u}_1\\ \tilde{u}_2\end{pmatrix}=\tilde{\eta}\begin{pmatrix}-\rho_1\sqrt{c_1^0}(1+O(\rho_1+r_0^{-2}))\\ 1\end{pmatrix}+O_{\rho_1}(\epsilon|\tilde{\eta}|+|\tilde{\eta}|^3)\begin{pmatrix}1\\0\end{pmatrix}. \tag{3.29}$$

Using (3.29) and (3.28), we find that the stable manifold $W_+^s(\epsilon)$ at $r=r_0$ is given by

$$\mathcal{W}_+^s(\epsilon)\mid_{r=r_0}\ :\ u=\sqrt{\epsilon}r_0\hat{\eta}\begin{pmatrix}-\sqrt{c_1^0}+O(\rho_1+r_0^{-2})+O_{\rho_1}(\epsilon+\sqrt{\epsilon}|\hat{\eta}|^2)\\ 0\end{pmatrix}+\hat{\eta}\begin{pmatrix}0\\1\end{pmatrix}.$$

We apply successive changes of variables to transform this expression into the $(A,B)$-coordinates and obtain

$$\begin{aligned}\mathcal{W}_+^s(\epsilon)\mid_{r=r_0}\ :\ &\begin{pmatrix}A\\B\end{pmatrix}=\\ &\epsilon\hat{\eta}\left[-\sqrt{c_1^0}+O(\rho_1+r_0^{-2})+O_{\rho_1}(\epsilon+\sqrt{\epsilon}|\hat{\eta}|^2)\right]\begin{pmatrix}r_0\\1\end{pmatrix}+\sqrt{\epsilon}\hat{\eta}\begin{pmatrix}1\\0\end{pmatrix}.\end{aligned} \tag{3.30}$$

We have now gathered all the results necessary for the proof of theorem 2.1. In order to do this, we need to find non-trivial intersections of the stable manifold $\mathcal{W}_+^s(\epsilon)$ with the center-unstable manifold $\mathcal{W}_-^{\mathrm{cu}}(\epsilon)$. To this end, we write the expansion (3.8) for each fixed $r_0 \gg 1$ in the $(\tilde{A},\tilde{B})$ coordinates and afterwards in the coordinates $(A,B)$. Using the expansions of Bessel functions and the variables $(d_1,d_2)=(\tilde{d}_1/\sqrt{r_0},\sqrt{r_0}\tilde{d}_2)$, we arrive at the expression

$$\begin{aligned}\begin{pmatrix}\tilde{A}\\ \tilde{B}\end{pmatrix}=&\mathrm{e}^{\mathrm{i}(r_0-\pi/4)}\begin{pmatrix}d_1(1+O(r_0^{-1}))+d_2(-\mathrm{i}+O(r_0^{-1}))\\ -d_2r_0^{-1}(\mathrm{i}+O(r_0^{-1}))-\left(\frac{1}{\sqrt{3}}+O(\frac{1}{\sqrt{r_0}})\right)\left(C_1\sqrt{r_0}d_1^2+\frac{C_2}{\sqrt{r_0}}d_1d_2\right)\end{pmatrix}\\ &+\mathrm{e}^{i(r_0-\pi/4)}\begin{pmatrix}O_{r_0}(\epsilon|d|+|d|^2)\\ O_{r_0}(\epsilon|d|+|d_2|^2+|d_1|^3)\end{pmatrix},\end{aligned} \tag{3.31}$$

with $C_1=\sqrt{2\pi}\mu_{\mathrm{c}}^2s_2((\Gamma_1+\Gamma_2)/4)$ and $C_2=-\sqrt{2\pi}\mu_{\mathrm{c}}^2s_2\Gamma_2$. We can apply the transformation (3.12) and obtain the expression

$$\begin{aligned}\mathcal{W}_-^{\mathrm{cu}}(\epsilon)\mid_{r=r_0}\ :\ \begin{pmatrix}A\\B\end{pmatrix}=&\mathrm{e}^{\mathrm{i}(-\pi/4+O(r_o^{-2})+O_{r_0}(\epsilon|d|+|d|^2)}\begin{pmatrix}O_{r_0}(\epsilon|d|+|d|^2)\\ O_{r_0}(\epsilon|d|+|d_2|^2+|d_1|^3)\end{pmatrix}\\ &+\mathrm{e}^{\mathrm{i}(-\frac{\pi}{4}+O(r_o^{-2})+O_{r_0}(\epsilon|d|+|d|^2)}\begin{pmatrix}d_1(1+O(r_0^{-1}))+d_2(-\mathrm{i}+O(r_0^{-1}))\\ -d_2r_0^{-1}(i+O(r_0^{-1}))\end{pmatrix}\\ &+\mathrm{e}^{\mathrm{i}(-\frac{\pi}{4}+O(r_o^{-2})+O_{r_0}(\epsilon|d|+|d|^2)}\begin{pmatrix}0\\ -\left(\frac{1}{\sqrt{3}}+O(\frac{1}{\sqrt{r_0}})\right)\left(C_1\sqrt{r_0}d_1^2+\frac{C_2}{\sqrt{r_0}}d_1d_2\right)\end{pmatrix}.\end{aligned} \tag{3.32}$$

After redefining $\hat{\eta}$ to $\eta$ to remove the phase in $\mathcal{W}_-^{\mathrm{cu}}(\epsilon)\mid_{r=r_0}$, it remains to solve

$$\sqrt{\epsilon}\eta+\epsilon r_0\eta\left[-\sqrt{c_1^0}+O(\rho_1+r_0^{-2})+O_{\rho_1}(\sqrt{\epsilon})\right]=d_1(1+O(r_0^{-1}))+d_2(-i+0(r_0^{-1}))+O_{r_0}$$
$$\times(\epsilon|d|+|d|^2),\epsilon\eta\left[-\sqrt{c_1^0}+O(\rho_1+r_0^{-2})+O_{\rho_1}(\sqrt{\epsilon})\right]=-d_2r_0^{-1}(i+O(r_0^{-1}))$$
$$+O_{r_0}(\epsilon|d|+|d_2|^2+|d_1|^3)-\left(\frac{1}{\sqrt{3}}+O(r_0^{-1/2})\right)\left(C_1\sqrt{r_0}d_1^2+\frac{C_2}{\sqrt{r_0}}d_1d_2\right).$$

Setting $d_j=\sqrt{\epsilon}\hat{d}_j$ and writing $\eta=\eta_1+i\eta_2$, we obtain

$$\hat{d}_1-\mathrm{i}\hat{d}_2-i\eta_2+O(r_0^{-1})\hat{d}+O_{r_0}(\epsilon|\hat{d}|+\sqrt{\epsilon}|\hat{d}|^2)=\eta_1+\sqrt{\epsilon}r_0O(\eta),$$

and

$$\sqrt{\epsilon}r_0\eta\left[-\sqrt{c_1^0}+O(\rho_1+r_0^{-2})+O_{\rho_1}(\sqrt{\epsilon})\right]=-\mathrm{i}\hat{d}_2+O(r_0^{-1})\hat{d}_2+O_{r_0}(\epsilon|\hat{d}|$$
$$+\sqrt{\epsilon}|\hat{d}_2|^2+\epsilon|\hat{d}_1|^3)-\left(\frac{1}{\sqrt{3}}+O(r_0^{-1/2})\right)\left(C_1r_0^{3/2}\sqrt{\epsilon}\hat{d}_1^2+C_2\sqrt{\epsilon}\sqrt{r_0}\hat{d}_1\hat{d}_2\right).$$

Hence, we find the expansion

$$\hat{d}_1=\eta_1+O_{r_0}(\sqrt{\epsilon}\eta_1),\quad \hat{d}_2=O_{r_0}(\sqrt{\epsilon}\eta_1),\quad \eta_2=O(r_0^{-1})\eta_1+O_{r_0}(\sqrt{\epsilon}\eta_1),$$

and we can solve the equation

$$\sqrt{\epsilon}r_0\eta_1\left[-\sqrt{c_1^0}+O(r_0^{-1})+O(\rho_1)+O_{\rho_1}(\sqrt{\epsilon})\right]$$
$$=-\left(\frac{1}{\sqrt{3}}+O(r_0^{-1/2})\right)C_1r_0^{3/2}\sqrt{\epsilon}\eta_1^2+O_{r_0}(\epsilon\eta_1),$$

that has two solutions $\eta_1=0$ (the trivial solution) and $\eta_1$ small given to leading order by

$$\eta_1=\frac{1}{C_1}\sqrt{\frac{3c_1^0}{r_0}}+O(\rho_1)+O(r_0^{-1})+O_{\rho_1}(\sqrt{\epsilon}).$$

This gives $\tilde{d}_1$ and $\tilde{d}_2$

$$\tilde{d}_1=\frac{s_1}{\mu_c^2s_2}\sqrt{\frac{3\epsilon}{2\pi c_1^0}},\quad \tilde{d}_2=O(\epsilon),$$

or equivalently ($\epsilon=-\lambda$, $c_1^0=-c_1^1$)

$$\tilde{d}_1=\frac{s_1}{\mu_c^2s_2}\sqrt{\frac{3\lambda}{2\pi c_1^1}},\quad \tilde{d}_2=O(\lambda).$$

This completes the proof of theorem 2.1.

### *3.2. Localized radial solutions in the Poincaré disc*

*3.2.1. Linear stability of the trivial state.* We look at the linearization of (2.11) about the trivial state $v=0$ governed by the equation

$$\partial_tu(z,t)=-u(z,t)+\mu s_1\int_{\mathbb{D}}W(d_{\mathbb{D}}(z,z'))u(z',t)\mathrm{dm}(z'). \tag{3.33}$$

Let $b$ be a point on the circle $\partial\mathbb{D}$. For $z\in\mathbb{D}$, we define the 'inner product' $\langle z,b\rangle$ as the algebraic distance to the origin of the (unique) horocycle based at $b$ and passing through $z$. This distance

is defined as the hyperbolic signed length of the segment $O\xi$ where $\xi$ is the intersection point of the horocycle and the line (geodesic) $Ob$. Looking at linear stability to periodic solutions on the Poincaré disc $u(z,t) = \mathrm{e}^{\sigma t}\mathrm{e}^{(\frac{1}{2}+\mathrm{i}\rho)\langle z,b\rangle}$ (see [27]) we obtain the following dispersion relation

$$\sigma(\rho) = -1 + \mu s_1 \mathcal{M}\mathbf{W}(\rho). \tag{3.34}$$

The critical value $\mu_c$ is then found to occur at

$$\mu_c = \frac{1}{s_1 \widetilde{W}_c}, \tag{3.35}$$

and for all $\mu < \mu_c$, the trivial solution $v = 0$ is stable.

We set $\lambda = \mu - \mu_c$ and rewrite equation (2.11)

$$\partial_t v(z,t) = \boldsymbol{L}_{\mu_c} v(z,t) + \boldsymbol{R}(v(z,t),\lambda), \tag{3.36}$$

where $\boldsymbol{L}_{\mu_c}$ and $\boldsymbol{R}$ are defined by

$$\begin{aligned}
\boldsymbol{L}_{\mu_c} v(z,t) &= -v(z,t) + \mu_c s_1 \int_{\mathbb{D}} W(d_{\mathbb{D}}(z,z'))v(z',t)\mathrm{dm}(z'),\\
\boldsymbol{R}(v(z,t),\lambda) &= \int_{\mathbb{D}} W(d_{\mathbb{D}}(z,z'))\left[S\left((\lambda+\mu_c)v(z',t)\right) - \mu_c s_1 v(z',t)\right]\mathrm{dm}(z'),
\end{aligned}$$

with $\boldsymbol{R}(0,0) = D_v\boldsymbol{R}(0,0) = 0$. We define $f(X,\lambda)$ by

$$f(X,\lambda) = S\left((\lambda+\mu_c)X\right) - \mu_c s_1 X,$$

where $f(0,0) = \partial_X f(0,0) = 0$.

*3.2.2. PDE methods in the Poincaré disc.* We assume that $v$ is a sufficiently smooth radially symmetric solution of equation (3.36) such that if we apply the Mehler–Fock transform we obtain

$$(\partial_t + 1)\,\mathcal{M}v(\rho,t) = \widetilde{W}(\rho)\left[\mu_c s_1 \mathcal{M}v(\rho,t) + \mathcal{M}f(v,\lambda)(\rho,t)\right].$$

We also assume that we can apply an inverse Mehler–Fock transform, to yield [43]

$$(\partial_t + 1)\left(1 + L^\tau_{\mathbb{D}}\right)^2 v = \Gamma_1 f(v,\lambda) - \Gamma_2 L^\tau_{\mathbb{D}} f(v,\lambda). \tag{3.37}$$

$L^\tau_{\mathbb{D}}$ has been defined in equation (2.16) and we have used the fact that

$$\begin{aligned}
\sigma_1^2\sigma_2^2 - \Gamma_1\mu_c s_1 &= 1,\\
\sigma_1^2 + \sigma_2^2 - \Gamma_2\mu_c s_1 &= -2.
\end{aligned}$$

We look for stationary radial solutions of equation (3.36), that is

$$\left(1 + L^\tau_{\mathbb{D}}\right)^2 v(\tau) = \Gamma_1 f(v(\tau),\lambda) - \Gamma_2 L^\tau_{\mathbb{D}} f(v(\tau),\lambda). \tag{3.38}$$

Note that $L^\tau_{\mathbb{D}} f(v(\tau),\lambda)$ can be expressed as

$$L^\tau_{\mathbb{D}} f(v,\lambda) = \left(L^\tau_{\mathbb{D}} v\right) f'(v,\lambda) + (\partial_\tau v)^2 f''(v,\lambda).$$

*3.2.3. The equation near the core.* We rewrite equation (3.38) as a four-dimensional system of non-autonomous differential equations to yield

$$\begin{aligned}
\partial_\tau u_1 &= u_3,\\
\partial_\tau u_2 &= u_4,\\
\left(\partial_\tau^2 + \coth(\tau)\partial_\tau + 1\right) u_1 &= u_2,\\
\left(\partial_\tau^2 + \coth(\tau)\partial_\tau + 1\right) u_2 &= \Gamma_1 f(u_1,\lambda) - \Gamma_2 L^\tau_{\mathbb{D}} f(u_1,\lambda),
\end{aligned}$$

and we may rewrite (3.38) as a spatial dynamical system

$$\partial_\tau U = \mathcal{A}(\tau)U + \mathcal{F}(U,\lambda), \tag{3.39}$$

where $U = (u_1, u_2, u_3, u_4)^{\mathrm{T}}$

$$\mathcal{A}(\tau) = \begin{pmatrix} 0 & 0 & 1 & 0 \\ 0 & 0 & 0 & 1 \\ -1 & 1 & -\coth(\tau) & 0 \\ 0 & -1 & 0 & -\coth(\tau) \end{pmatrix} \text{ and,}$$

$$\mathcal{F}(U,\lambda) = \begin{pmatrix} 0 \\ 0 \\ 0 \\ \mathcal{F}_4\left(u_1,u_2,u_3,u_4,\lambda\right), \end{pmatrix}$$

and

$$\mathcal{F}_4\left(u_1,u_2,u_3,u_4,\lambda\right) = \Gamma_1 f(u_1,\lambda) - \Gamma_2\left[(u_2-u_1)f'(u_1,\lambda) + u_3^2 f''(u_1,\lambda)\right].$$

First, we set $\lambda = 0$ and linearize (3.39) about $U = 0$ to get the linear system $\partial_\tau U = \mathcal{A}(\tau)U$. Proposition 3.1 defines the four linearly independent solutions of the linear system $\partial_\tau U = \mathcal{A}(\tau)U$.

**Proposition 3.1.** *The linear system $\partial_\tau U = \mathcal{A}(\tau)U$ has four linearly independent solutions given by*

$$\begin{aligned} V_1(\tau) &= \left(\mathcal{P}_\nu(\cosh\tau), 0, \mathcal{P}_\nu^1(\cosh\tau), 0\right)^{\mathrm{T}}, \\ V_2(\tau) &= \left(V_2^1(\tau), \mathcal{P}_\nu(\cosh\tau), V_2^3(\tau), \mathcal{P}_\nu^1(\cosh\tau),\right)^{\mathrm{T}} \\ V_3(\tau) &= \left(\mathcal{Q}_\nu(\cosh\tau), 0, \mathcal{Q}_\nu^1(\cosh\tau), 0\right)^{\mathrm{T}}, \\ V_4(\tau) &= \left(V_4^1(\tau), \mathcal{Q}_\nu(\cosh\tau), V_4^3(\tau), \mathcal{Q}_\nu^1(\cosh\tau)\right)^{\mathrm{T}}, \end{aligned}$$

*where*

$$\nu = -\frac{1}{2} + \mathrm{i}\frac{\sqrt{3}}{2} \tag{3.40}$$

*and*

$$\begin{aligned} V_2^1(\tau) &= \mathcal{P}_\nu(\cosh\tau)\int_0^\tau \mathcal{P}_\nu(\cosh s)\mathcal{Q}_\nu(\cosh s)\sinh(s)\,\mathrm{d}s \\ &\quad - \mathcal{Q}_\nu(\cosh\tau)\int_0^\tau (\mathcal{P}_\nu(\cosh s))^2\sinh(s)\,\mathrm{d}s, \\ V_2^3(\tau) &= \mathcal{P}_\nu^1(\cosh\tau)\int_0^\tau \mathcal{P}_\nu(\cosh s)\mathcal{Q}_\nu(\cosh s)\sinh(s)\,\mathrm{d}s \\ &\quad - \mathcal{Q}_\nu^1(\cosh\tau)\int_0^\tau (\mathcal{P}_\nu(\cosh s))^2\sinh(s)\,\mathrm{d}s, \\ V_4^1(\tau) &= \mathcal{P}_\nu(\cosh\tau)\int_0^\tau (\mathcal{Q}_\nu(\cosh s))^2\sinh(s)\,\mathrm{d}s \\ &\quad - \mathcal{Q}_\nu(\cosh\tau)\int_0^\tau \mathcal{P}_\nu(\cosh s)\mathcal{Q}_\nu(\cosh s)\sinh(s)\,\mathrm{d}s, \\ V_4^3(\tau) &= \mathcal{P}_\nu^1(\cosh\tau)\int_0^\tau (\mathcal{Q}_\nu(\cosh s))^2\sinh(s)\,\mathrm{d}s \\ &\quad - \mathcal{Q}_\nu^1(\cosh\tau)\int_0^\tau \mathcal{P}_\nu(\cosh s)\mathcal{Q}_\nu(\cosh s)\sinh(s)\,\mathrm{d}s. \end{aligned}$$

**Proof.** From equation (2.13), the associated Legendre functions $\mathcal{P}_\nu(\cosh\cdot)$ and $\mathcal{Q}_\nu(\cosh\cdot)$ form a basis of solutions for the equation

$$\partial_\tau^2\Psi(\tau) + \coth(\tau)\partial_\tau\Psi(\tau) - \nu(\nu+1)\Psi(\tau) = 0.$$

If $\nu = -\frac{1}{2} + \mathrm{i}\frac{\sqrt{3}}{2}$ then we have $\nu(\nu+1) = -1$. This implies that $\mathcal{P}_{-\frac{1}{2}+\mathrm{i}\frac{\sqrt{3}}{2}}(\cosh\tau)$ and $\mathcal{Q}_{-\frac{1}{2}+\mathrm{i}\frac{\sqrt{3}}{2}}(\cosh\tau)$ are solutions of

$$\partial_\tau^2\Psi(\tau) + \coth(\tau)\partial_\tau\Psi(\tau) + \Psi(\tau) = 0.$$

Hence we set $\nu = -\frac{1}{2} + \mathrm{i}\frac{\sqrt{3}}{2}$. The solution of the linear system $\partial_\tau U = \mathcal{A}(\tau)U$ can be found by inspecting the equivalent system

$$\left(\partial_\tau^2 + \coth(\tau)\partial_\tau + 1\right)u_1 = u_2, \quad \left(\partial_\tau^2 + \coth(\tau)\partial_\tau + 1\right)u_2 = 0.$$

Consequently, solutions $V_1(\tau) = \left(\mathcal{P}_\nu(\cosh\tau), 0, \mathcal{P}_\nu^1(\cosh\tau), 0\right)^{\mathrm{T}}$ and $V_3(\tau) = \left(\mathcal{Q}_\nu(\cosh\tau), 0, \mathcal{Q}_\nu^1(\cosh\tau), 0\right)^{\mathrm{T}}$ are found to be two linearly independent solutions, where we have used the relations

$$\partial_\tau\left(\mathcal{P}_\nu(\cosh\tau)\right) = \mathcal{P}_\nu^1(\cosh\tau), \quad \partial_\tau\left(\mathcal{Q}_\nu(\cosh\tau)\right) = \mathcal{Q}_\nu^1(\cosh\tau).$$

In order to find the other two linearly independent solutions, we have to solve the equation

$$\left(\partial_\tau^2 + \coth\tau\,\partial_\tau + 1\right)u(\tau) = \mathcal{P}_\nu(\cosh\tau).$$

Searching for solutions of the form $u(\tau) = c_1(\tau)\mathcal{P}_\nu(\cosh\tau) + c_2(\tau)\mathcal{Q}_\nu(\cosh\tau)$, we find that $c_1(\tau)$ and $c_2(\tau)$ satisfy the system

$$\begin{aligned}&\dot{c}_1(\tau)\mathcal{P}_\nu(\cosh\tau) + \dot{c}_2(\tau)\mathcal{Q}_\nu(\cosh\tau) = 0,\\ &\dot{c}_1(\tau)\mathcal{P}_\nu^1(\cosh\tau) + \dot{c}_2(\tau)\mathcal{Q}_\nu^1(\cosh\tau) = \mathcal{P}_\nu(\cosh\tau),\end{aligned} \tag{3.41}$$

where dots denote derivatives with respect to $\tau$. Rewriting (3.41) in matrix form yields

$$\begin{pmatrix}\mathcal{P}_\nu(\cosh\tau) & \mathcal{Q}_\nu(\cosh\tau)\\ \mathcal{P}_\nu^1(\cosh\tau) & \mathcal{Q}_\nu^1(\cosh\tau)\end{pmatrix}\begin{pmatrix}\dot{c}_1(\tau)\\ \dot{c}_2(\tau)\end{pmatrix} = \begin{pmatrix}0\\ \mathcal{P}_\nu(\cosh\tau)\end{pmatrix}, \tag{3.42}$$

and from formula in [39, page 123], we obtain that

$$W(\tau) = \mathcal{P}_\nu(\cosh\tau)\mathcal{Q}_\nu^1(\cosh\tau) - \mathcal{P}_\nu^1(\cosh\tau)\mathcal{Q}_\nu(\cosh\tau) = -\frac{1}{\sinh\tau},$$

where $W(\tau)$ is non-vanishing for all $\tau \in ]0; +\infty[$ such that we can invert the matrix system on left hand side of (3.42) to obtain:

$$\begin{aligned}\dot{c}_1(\tau) &= \sinh\tau\,\mathcal{P}_\nu(\cosh\tau)\mathcal{Q}_\nu(\cosh\tau),\\ \dot{c}_2(\tau) &= -\sinh\tau\,\left(\mathcal{P}_\nu(\cosh\tau)\right)^2.\end{aligned}$$

Hence we have

$$\begin{aligned}u(\tau) = c_1\mathcal{P}_\nu(\cosh\tau) + c_2\mathcal{Q}_\nu(\cosh\tau) + \mathcal{P}_\nu(\cosh\tau)\int_0^\tau \mathcal{P}_\nu(\cosh s)\mathcal{Q}_\nu(\cosh s)\sinh(s)\,\mathrm{d}s\\ -\mathcal{Q}_\nu(\cosh\tau)\int_0^\tau \left(\mathcal{P}_\nu(\cosh s)\right)^2\sinh(s)\,\mathrm{d}s,\end{aligned}$$

where $c_1, c_2 \in \mathbb{R}$ are two constants. Equivalently, the solutions of

$$\left(\partial_\tau^2 + \coth\tau\,\partial_\tau + 1\right)u(\tau) = \mathcal{Q}_\nu(\cosh\tau)$$

are given by

$$\begin{aligned}u(\tau) = c_3\mathcal{P}_\nu(\cosh\tau) + c_4\mathcal{Q}_\nu(\cosh\tau) + \mathcal{P}_\nu(\cosh\tau)\int_0^\tau \left(\mathcal{Q}_\nu(\cosh s)\right)^2\sinh(s)\,\mathrm{d}s\\ -\mathcal{Q}_\nu(\cosh\tau)\int_0^\tau \mathcal{P}_\nu(\cosh s)\mathcal{Q}_\nu(\cosh s)\sinh(s)\,\mathrm{d}s,\end{aligned}$$

**Table 1.** Expansions of associated Legendre functions $\mathcal{P}_\nu^k(\cosh\cdot)$ and $\mathcal{Q}_\nu^k(\cosh\cdot)$ for $\tau \to 0$ and $\tau \to \infty$; see [39, 96]. $C_0$, $C_1$, $\Phi_0$ and $\Phi_1$ are all real constants given in proposition 3.2.

| | $\tau \to 0$ | $\tau \to \infty$ |
|---|---|---|
| $\mathcal{P}_\nu(\cosh\cdot)$ | $1 + O(\tau^2)$ | $C_0 \cos\left(\frac{\sqrt{3}\tau}{2} + \Phi_0\right) \mathrm{e}^{-\frac{\tau}{2}} + O\left(\mathrm{e}^{-\frac{3\tau}{2}}\right)$ |
| $\mathcal{P}_\nu^1(\cosh\cdot)$ | $\tau\left(-\frac{1}{2} + O(\tau^2)\right)$ | $C_0 \cos\left(\frac{\sqrt{3}\tau}{2} + \Phi_0 + \frac{2\pi}{3}\right) \mathrm{e}^{-\frac{\tau}{2}} + O\left(\mathrm{e}^{-\frac{3\tau}{2}}\right)$ |
| $\mathcal{Q}_\nu(\cosh\cdot)$ | $(-1 + O(\tau^2))\ln\tau + O(1)$ | $C_1 \cos\left(\frac{\sqrt{3}\tau}{2} - \Phi_1\right) \mathrm{e}^{-\frac{\tau}{2}} + O\left(\mathrm{e}^{-\frac{3\tau}{2}}\right)$ |
| $\mathcal{Q}_\nu^1(\cosh\cdot)$ | $(1 + O(\tau^2))\tau\ln\tau - \frac{1}{\tau} + O(1)$ | $C_1 \cos\left(\frac{\sqrt{3}\tau}{2} - \Phi_1 + \frac{2\pi}{3}\right) \mathrm{e}^{-\frac{\tau}{2}} + O\left(\mathrm{e}^{-\frac{3\tau}{2}}\right)$ |

with constants $c_3, c_4 \in \mathbb{R}$.

Choosing linearly independent solutions, we finally obtain the result stated in the proposition. □

In table 1, we summarize the expansions of the associated Legendre functions in the limits $\tau \to 0$ and $\tau \to \infty$; proposition 3.2 defines the constants in the $\tau \to \infty$ limit. Thus, $V_1(\tau)$ and $V_2(\tau)$ stay bounded as $\tau \to 0$, while the norms of $V_3(\tau)$ and $V_4(\tau)$ behave like $\ln\tau$ as $\tau \to 0$. We expect that the set of solutions of (3.39) that are bounded as $\tau \to 0$ forms a two-dimensional manifold in $\mathbb{R}^4$ for each fixed $\tau > 0$. We denote the projection $P_-^{\mathrm{cu}}(\tau_0)$ onto the space spanned by $V_1(\tau_0)$, $V_2(\tau_0)$ with null space given by the span of $V_3(\tau_0)$, $V_4(\tau_0)$.

**Proposition 3.2.** *The constants $C_0$, $C_1$, $\Phi_0$ and $\Phi_1$, given in table 1, are*

$$C_0 = 2\sqrt{\frac{2\sqrt{3}}{3\pi\tanh\left(\frac{\sqrt{3}\pi}{2}\right)}} \qquad \text{and} \qquad C_1 = \sqrt{\frac{2\pi\sqrt{3}\tanh\left(\frac{\sqrt{3}\pi}{2}\right)}{3}}, \tag{3.43}$$

$$\Phi_0 = \arg\left(\frac{\Gamma\left(\mathrm{i}\frac{\sqrt{3}}{2}\right)}{\Gamma\left(\frac{1}{2} + \mathrm{i}\frac{\sqrt{3}}{2}\right)}\right) \qquad \text{and} \qquad \Phi_0 + \Phi_1 = -\frac{\pi}{2}. \tag{3.44}$$

**Proof.** The proof of this proposition is based on the asymptotics as $z \to \infty$ [94]

$$\mathcal{P}_\nu^m(z) \approx \frac{z^{m/2}}{\sqrt{\pi}(z-1)^{m/2}}\left(\frac{(2z)^\nu\Gamma(\nu+1/2)}{\Gamma(\nu-m+1)}\left(1+O(z^{-1})\right)\right.$$
$$\left. + \frac{(2z)^{-\nu-1}\Gamma(-\nu-1/2)}{\Gamma(-m-\nu)}\left(1+O(z^{-1})\right)\right),$$

and

$$\mathcal{Q}_\nu^m(z) \approx \frac{2^{-\nu-2}z^{-\nu-1}}{\sqrt{\pi}\Gamma(-m-\nu)\Gamma(\nu-m+1)}\left(\frac{1+z}{z-1}\right)^{m/2}\left(\vphantom{\frac{1}{1}}(2z)^{2\nu+1}\Gamma(-m-\nu)\Gamma(\nu+1/2)\right.$$
$$\times\left(\ln(1+z)-\ln(z-1)\right)\left(1+O(z^{-1})\right) + \Gamma(-m+\nu+1)\Gamma(-\nu-1/2)$$
$$\left.\times\ (2\pi+\ln(1+z)-\ln(z-1))\left(1+O(z^{-1})\right)\right).$$

We directly obtain the identities

$$C_0 = \frac{2}{\sqrt{\pi}}\left|\frac{\Gamma\left(\mathrm{i}\frac{\sqrt{3}}{2}\right)}{\Gamma\left(\frac{1}{2}+\mathrm{i}\frac{\sqrt{3}}{2}\right)}\right|, \quad \Phi_0 = \arg\left(\frac{\Gamma\left(\mathrm{i}\frac{\sqrt{3}}{2}\right)}{\Gamma\left(\frac{1}{2}+\mathrm{i}\frac{\sqrt{3}}{2}\right)}\right),$$
$$C_1 = \sqrt{\pi}\left|\cot\left(\pi\left(-\frac{1}{2}+\mathrm{i}\frac{\sqrt{3}}{2}\right)\right)\frac{\Gamma\left(\mathrm{i}\frac{\sqrt{3}}{2}\right)}{\Gamma\left(\frac{1}{2}+\mathrm{i}\frac{\sqrt{3}}{2}\right)}\right|,$$
$$\Phi_1 = \arg\left[\sqrt{\pi}\cot\left(\pi\left(-\frac{1}{2}+\mathrm{i}\frac{\sqrt{3}}{2}\right)\right)\frac{\Gamma\left(\mathrm{i}\frac{\sqrt{3}}{2}\right)}{\Gamma\left(\frac{1}{2}+\mathrm{i}\frac{\sqrt{3}}{2}\right)}\right].$$

The formulas for $C_0$ and $C_1$ are obtained by the standard identity involving the Gamma function

$$\left|\frac{\Gamma\left(\mathrm{i}\frac{\sqrt{3}}{2}\right)}{\Gamma\left(\frac{1}{2}+\mathrm{i}\frac{\sqrt{3}}{2}\right)}\right| = \sqrt{\frac{2\sqrt{3}}{3\tanh\left(\frac{\sqrt{3}\pi}{2}\right)}}.$$

The formula (3.43) is then obtained from the above equation. The second relation in (3.44) can be verified from the above expressions of $\Phi_0$ and $\Phi_1$. □

**Remark 3.1.** *One can deduce from (3.43) the following identity*

$$\frac{\sqrt{3}C_0}{6} = \frac{C_1C_0^2}{8}. \tag{3.45}$$

We are now able to present the hyperbolic equivalent of lemma 3.1 for the centre-unstable manifold $\mathcal{W}_-^{\mathrm{cu}}$.

**Lemma 3.4.** *Fix $\tau_0 > 0$, then there exist constants $\delta_0, \delta_1$ such that the set $\mathcal{W}_-^{\mathrm{cu}}(\lambda)$ of solutions $U(\tau)$ of (3.39) for which $\sup_{0\leqslant\tau\leqslant\tau_0}|U(\tau)| < \delta_0$ is, for $|\lambda| < \delta_0$, is a smooth two-dimensional manifold. Furthermore, $U \in \mathcal{W}_-^{\mathrm{cu}}(\lambda)$ with $|P_-^{\mathrm{cu}}(\tau_0)U(\tau_0)| < \delta_1$ if and only if*

$$U(\tau_0) = \tilde{d}_1V_1(\tau_0) + \tilde{d}_2V_2(\tau_0) + V_3(\tau_0)O_{\tau_0}(|\lambda||\tilde{d}| + |\tilde{d}|^2) + V_4(\tau_0)$$
$$\times\left(\Xi_{\tilde{d}_1^2}\tilde{d}_1^2 + \Xi_{\tilde{d}_1\tilde{d}_2}\tilde{d}_1\tilde{d}_2 + O_{\tau_0}(|\lambda||\tilde{d}| + |\tilde{d}_2|^2 + |\tilde{d}|^3)\right), \tag{3.46}$$

*where*

$$\Xi_{\tilde{d}_1^2} = \frac{\mu_c^2 s_2}{2}\left[-(\Gamma_1+2\Gamma_2)\mathcal{I}_1 + 2\Gamma_2\mathcal{I}_2 + o(1)\right],$$
$$\Xi_{\tilde{d}_1\tilde{d}_2} = \mu_c^2 s_2\left[\Gamma_2\mathcal{I}_1 + o(1)\right],$$

*with*

$$\mathcal{I}_1 = \int_0^\infty (\mathcal{P}_\nu(\cosh s))^3\sinh s\,\mathrm{d}s < \infty,$$
$$\mathcal{I}_2 = \int_0^\infty \mathcal{P}_\nu(\cosh s)\left(\mathcal{P}_\nu^1(\cosh s)\right)^2\sinh s\,\mathrm{d}s < \infty.$$

*for some $\tilde{d} = (\tilde{d}_1, \tilde{d}_2) \in \mathbb{R}^2$ with $|\tilde{d}| < \delta_1$, where the right-hand side in (3.46) depends smoothly on $(\tilde{d}, \lambda)$.*

**Proof.** The proof is similar to that of lemma 3.1. We observe that four independent solutions to the adjoint problem $\partial_\tau U = -\mathcal{A}^{\mathrm{T}}(\tau)U$ are given by

$$\begin{aligned}
W_1(\tau) &= \sinh\tau\left(\mathcal{Q}_\nu^1(\cosh\tau), W_1^2(\tau), -\mathcal{Q}_\nu(\cosh\tau), W_1^4(\tau)\right)^{\mathrm{T}},\\
W_2(\tau) &= \sinh\tau\left(0, \mathcal{Q}_\nu^1(\cosh\tau), 0, -\mathcal{Q}_\nu(\cosh\tau)\right)^{\mathrm{T}},\\
W_3(\tau) &= \sinh\tau\left(\mathcal{P}_\nu^1(\cosh\tau), W_3^2(\tau), -\mathcal{P}_\nu(\cosh\tau), W_3^4(\tau)\right)^{\mathrm{T}}\\
W_4(\tau) &= \sinh\tau\left(0, \mathcal{P}_\nu^1(\cosh\tau), 0, -\mathcal{P}_\nu(\cosh\tau)\right)^{\mathrm{T}},
\end{aligned}$$

where

$$\begin{aligned}
W_1^2(\tau) &= \mathcal{P}_\nu^1(\cosh\tau)\int_0^\tau \mathcal{P}_\nu^1(\cosh s)\mathcal{Q}_\nu^1(\cosh s)\sinh(s)\,\mathrm{d}s - \mathcal{Q}_\nu^1(\cosh\tau)\\
&\quad\times\int_0^\tau\left(\mathcal{P}_\nu^1(\cosh s)\right)^2\sinh(s)\,\mathrm{d}s,\\
W_1^4(\tau) &= -\mathcal{Q}_\nu(\cosh\tau) - \mathcal{P}_\nu(\cosh\tau)\int_0^\tau \mathcal{P}_\nu^1(\cosh s)\mathcal{Q}_\nu^1(\cosh s)\sinh(s)\,\mathrm{d}s + \mathcal{Q}_\nu(\cosh\tau)\\
&\quad\times\int_0^\tau\left(\mathcal{P}_\nu^1(\cosh s)\right)^2\sinh(s)\,\mathrm{d}s,\\
W_3^2(\tau) &= \mathcal{P}_\nu^1(\cosh\tau)\int_0^\tau\left(\mathcal{Q}_\nu^1(\cosh s)\right)^2\sinh(s)\,\mathrm{d}s - \mathcal{Q}_\nu^1(\cosh\tau)\\
&\quad\times\int_0^\tau \mathcal{P}_\nu^1(\cosh s)\mathcal{Q}_\nu^1(\cosh s)\sinh(s)\,\mathrm{d}s,\\
W_3^4(\tau) &= -\mathcal{P}_\nu(\cosh\tau) - \mathcal{P}_\nu(\cosh\tau)\int_0^\tau\left(\mathcal{Q}_\nu^1(\cosh s)\right)^2\sinh(s)\,\mathrm{d}s - \mathcal{Q}_\nu(\cosh\tau)\\
&\quad\times\int_0^\tau \mathcal{P}_\nu^1(\cosh s)\mathcal{Q}_\nu^1(\cosh s)\sinh(s)\,\mathrm{d}s.
\end{aligned}$$

The calculation of $W_i(\tau)$ uses the following facts:

- the following relations are satisfied [39]:

$$\begin{aligned}
\partial_\tau\left(\sinh\tau\mathcal{P}_\nu^1(\cosh\tau)\right) &= -\sinh\tau\mathcal{P}_\nu(\cosh\tau),\\
\partial_\tau\left(\sinh\tau\mathcal{Q}_\nu^1(\cosh\tau)\right) &= -\sinh\tau\mathcal{Q}_\nu(\cosh\tau),
\end{aligned}$$

- the solutions of

$$\begin{aligned}
\left(\partial_\tau^2 - \coth\tau\,\partial_\tau + 1\right)q_1(\tau) &= \sinh\tau\mathcal{P}_\nu^1(\cosh\tau),\\
\left(\partial_\tau^2 - \coth\tau\,\partial_\tau + 1\right)q_2(\tau) &= \sinh\tau\mathcal{Q}_\nu^1(\cosh\tau),
\end{aligned}$$

  are given by

$$\begin{aligned}
q_1(\tau) &= c_1\sinh\tau\mathcal{P}_\nu^1(\cosh\tau) + c_2\sinh\tau\mathcal{Q}_\nu^1(\cosh\tau)\\
&\quad+\sinh\tau\mathcal{P}_\nu^1(\cosh\tau)\int_0^\tau \mathcal{P}_\nu^1(\cosh s)\mathcal{Q}_\nu^1(\cosh s)\sinh(s)\,\mathrm{d}s\\
&\quad-\sinh\tau\mathcal{Q}_\nu^1(\cosh\tau)\int_0^\tau\left(\mathcal{P}_\nu^1(\cosh s)\right)^2\sinh(s)\,\mathrm{d}s,\\
q_2(\tau) &= c_3\sinh\tau\mathcal{P}_\nu^1(\cosh\tau) + c_4\sinh\tau\mathcal{Q}_\nu^1(\cosh\tau) + \sinh\tau\mathcal{P}_\nu^1(\cosh\tau)\\
&\quad\times\int_0^\tau\left(\mathcal{Q}_\nu^1(\cosh s)\right)^2\sinh(s)\,\mathrm{d}s - \sinh\tau\mathcal{Q}_\nu^1(\cosh\tau)\\
&\quad\times\int_0^\tau \mathcal{P}_\nu^1(\cosh s)\mathcal{Q}_\nu^1(\cosh s)\sinh(s)\,\mathrm{d}s,
\end{aligned}$$

with four real constants $c_1, c_2, c_3, c_4 \in \mathbb{R}$.

It follows from

$$\sinh\tau\left(\mathcal{P}_\nu^1(\cosh\tau)\mathcal{Q}_\nu(\cosh\tau)-\mathcal{P}_\nu(\cosh\tau)\mathcal{Q}_\nu^1(\cosh\tau)\right)=1,$$

that

$$\langle V_i(\tau), W_j(\tau)\rangle_{\mathbb{R}^4}=\delta_{i,j}\quad i,j=1,\ldots,4,$$

is independent of $\tau$. For a given $\tilde{d}=(\tilde{d}_1,\tilde{d}_2)\in\mathbb{R}^2$, we consider the fixed-point equation:

$$\begin{aligned}U(\tau)=&\sum_{j=1}^{2}\tilde{d}_jV_j(\tau)+\sum_{j=1}^{2}V_j(\tau)\int_{\tau_0}^{\tau}\langle W_j(s),\mathcal{F}(U(s),\lambda)\rangle\,\mathrm{d}s+\sum_{j=3}^{4}V_j(\tau)\\&\times\int_0^{\tau}\langle W_j(s),\mathcal{F}(U(s),\lambda)\rangle\,\mathrm{d}s=\sum_{j=1}^{2}\tilde{d}_jV_j(\tau)+\sum_{j=1}^{2}V_j(\tau)\\&\times\int_{\tau_0}^{\tau}W_{j,4}(s)\mathcal{F}_4(U(s),\lambda)\,\mathrm{d}s+\sum_{j=3}^{4}V_j(\tau)\int_0^{\tau}W_{j,4}(s)\mathcal{F}_4(U(s),\lambda)\,\mathrm{d}s\end{aligned}\tag{3.47}$$

on $\mathcal{C}^0([0,\tau_0],\mathbb{R}^4)$, where $W_{j,4}(\tau)$ (respectively $\mathcal{F}_4(U(\tau),\lambda)$) denotes the fourth component of $W_j(\tau)$ (respectively $\mathcal{F}(U(\tau),\lambda)$).

Hence, we have that:

- Each solution $U\in\mathcal{C}^0([0,\tau_0],\mathbb{R}^4)$ of (3.47) gives a solution of (3.39) that is bounded on $[0,\tau_0]$.
- Every bounded solution $U\in\mathcal{C}^0([0,\tau_0],\mathbb{R}^4)$ of (3.39) satisfies (3.47) provided that we add $\tilde{d}_3V_3(\tau)+\tilde{d}_4V_4(\tau)$ to the right-hand side for an appropriate $\tilde{d}\in\mathbb{R}^4$.
- Existence of solutions of (3.47) is given by the uniform contraction mapping principle for sufficiently small $(\tilde{d}_1,\tilde{d}_2)$ and $\lambda$.
- The resulting solution $U$ satisfies $U(\tau)=\sum_{j=1}^{2}\tilde{d}_jV_j(\tau)+O_{\tau_0}(|\lambda||\tilde{d}|+|\tilde{d}|^2)$ on $[0,\tau_0]$.

We also need to compute the quadratic coefficient in $\tilde{d}$ in front of $V_4(\tau_0)$, denoted by $\Xi$. The quadratic term in $U$ of $\mathcal{F}(U,\lambda)$ at $(0,0)$ is given by

$$\mathcal{F}_{20}(U,U)=\frac{\mu_c^2s_2}{2}\left(0,0,0,(\Gamma_1+2\Gamma_2)u_1^2-2\Gamma_2u_1u_2-2\Gamma_2u_3^2\right)^{\mathrm{T}}.$$

If we evaluate (3.47) at $\tau=\tau_0$, we arrive at (3.46) except that we need to calculate the quadratic coefficients in front of $V_4(\tau_0)$. Using a Taylor expansion, we find that these coefficients are given by

$$\Xi_{\tilde{d}_1^2}=\frac{\mu_c^2s_2}{2}\int_0^{\tau_0}W_{4,4}(s)\left[(\Gamma_1+2\Gamma_2)\left(\mathcal{P}_\nu(\cosh s)\right)^2-2\Gamma_2\left(\mathcal{P}_\nu^1(\cosh s)\right)^2\right]\mathrm{d}s,$$

and

$$\Xi_{\tilde{d}_1\tilde{d}_2}=-\mu_c^2s_2\Gamma_2\int_0^{\tau_0}W_{4,4}(s)\left(\mathcal{P}_\nu(\cosh s)\right)^2\,\mathrm{d}s.$$

Hence, we have

$$\begin{aligned}\Xi_{\tilde{d}_1^2}&=\frac{\mu_c^2s_2}{2}\left[-(\Gamma_1+2\Gamma_2)\mathcal{I}_1+2\Gamma_2\mathcal{I}_2+o(1)\right]\\\Xi_{\tilde{d}_1\tilde{d}_2}&=\mu_c^2s_2\left[\Gamma_2\mathcal{I}_1+o(1)\right],\end{aligned}$$

where

$$\mathcal{I}_1 = \int_0^\infty (\mathcal{P}_\nu(\cosh s))^3 \sinh s \mathrm{d}s < \infty,$$
$$\mathcal{I}_2 = \int_0^\infty \mathcal{P}_\nu(\cosh s) \left(\mathcal{P}_\nu^1(\cosh s)\right)^2 \sinh s \mathrm{d}s < \infty.$$

□

*3.2.4. The far-field equations and matching.* We make spatial dynamical system (3.39) autonomous by augmenting the system with the equation $\partial_\tau \alpha = -\alpha(2+\alpha)$ where $\alpha = \coth \tau - 1$ to yield the new system

$$\frac{\mathrm{d}}{\mathrm{d}\tau}\begin{pmatrix} u_1 \\ u_2 \\ u_3 \\ u_4 \\ \alpha \end{pmatrix} = \begin{pmatrix} u_3 \\ u_4 \\ -u_1 + u_2 - (1+\alpha)u_3 \\ -u_2 - (1+\alpha)u_4 + \mathcal{F}_4\,(u_1, u_2, u_3, u_4, \lambda, \alpha) \\ -\alpha(2+\alpha) \end{pmatrix}. \tag{3.48}$$

In the remainder of this section, we focus on the regime $\alpha \approx 0$ which corresponds to the far field $\tau \gg 1$. We denote $\mathcal{A}(\infty, \lambda)$ by the matrix

$$\mathcal{A}(\infty, \lambda) = \begin{pmatrix} 0 & 0 & 1 & 0 \\ 0 & 0 & 0 & 1 \\ -1 & 1 & -1 & 0 \\ s_1(\Gamma_1 + \Gamma_2)\lambda & -1 - s_1\Gamma_2\lambda & 0 & -1 \end{pmatrix},$$

where $\partial_\tau U = \mathcal{A}(\tau, \lambda)U$ is the linearization of (3.48) about the trivial state. We find that the matrix $\mathcal{A}(\infty, 0)$ has four eigenvalues $\nu, \bar{\nu}$ with multiplicity two ($\nu$ is defined in equation (3.40); see figure 2. As $\Re(\nu) = -1/2$, the trivial state $U = 0$ is asymptotically stable at $\lambda = 0$ and then there is no bifurcation at the far field. Recall that in the Euclidean case a Turing instability occurs at infinity. In figure 2, we summarize how the eigenvalues $\ell$ of $\mathcal{A}(\infty, \lambda)$ split close to $\lambda = 0$. For $\lambda > 0$, there exist four complex conjugate eigenvalues with $\Re(\ell) = -1/2$. For $\lambda < 0$, there exist four complex conjugate eigenvalues with $\Re(\ell) \neq -1/2$ and stable manifold $\mathcal{W}_+^s$ is the union of the stable fast manifold (which we denote by $\mathcal{W}_+^{\mathrm{sf}}$) and the stable slow manifold (which we denote by $\mathcal{W}_+^{\mathrm{ss}}$) corresponding to the fast and slow decay to the trivial state.

First we argue that the centre-unstable manifold $\mathcal{W}_-^{\mathrm{cu}}$ and stable manifold $\mathcal{W}_+^s$ should intersect. We have that $V_1(\tau)$ and $V_3(\tau)$ decay like $\mathrm{e}^{-\tau/2}$, while $V_2(\tau)$ and $V_4(\tau)$ decay like $\tau \mathrm{e}^{-\tau/2}$ as $\tau \to \infty$. Hence the tangent space of the stable manifold at $(u, \lambda) = 0$ is spanned by $(V_1(\tau), V_2(\tau), V_3(\tau), V_4(\tau))$. On the other hand, we showed in lemma 3.4 that the tangent space of the core manifold is spanned by $V_1(\tau)$ and $V_2(\tau)$. Then these tangent spaces would intersect along the two-dimensional subspace spanned by $V_1(\tau)$ and $V_2(\tau)$.

In order to show that the centre-unstable manifold $\mathcal{W}_-^{\mathrm{cu}}$ intersects the stable fast manifold $\mathcal{W}_+^{\mathrm{sf}}$, we need to find an explicit description of $\mathcal{W}_+^{\mathrm{sf}}$. To do this, we use successive, well chosen changes of variables to put (3.48) into normal form. We first define the linear change of coordinates

$$U = \widetilde{A}\begin{pmatrix} 1 \\ 0 \\ \nu \\ 0 \end{pmatrix} + \widetilde{B}\begin{pmatrix} 0 \\ 2\nu + 1 \\ 1 \\ \nu(2\nu+1) \end{pmatrix} + \text{c.c.},$$

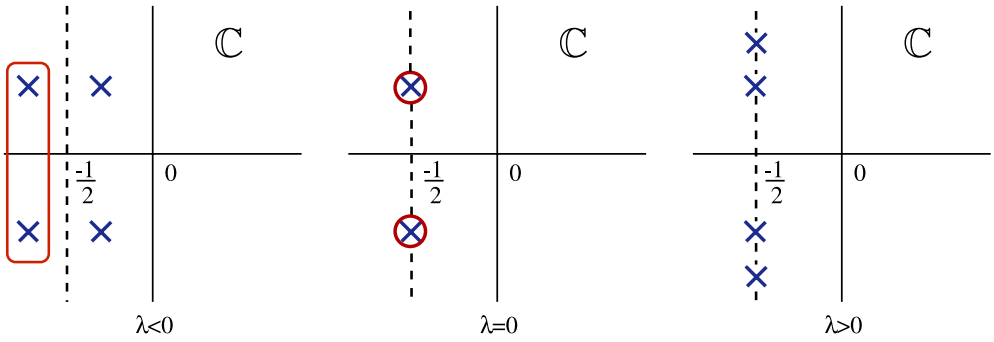


**Figure 2.** Schematic splitting of the eigenvalues $\ell$ of $\mathcal{A}(\infty,\lambda)$ for different values of $\lambda$. At $\lambda=0$, the multiplicity is two. Eigenvalues in the red box correspond to the stable fast manifold $\mathcal{W}_+^{\mathrm{sf}}(\lambda)$.

or equivalently,

$$\begin{pmatrix}\widetilde{A}\\ \widetilde{B}\end{pmatrix}=\begin{pmatrix}\frac{1}{2}u_1+\mathrm{i}\frac{\sqrt{3}}{3}\left(-\frac{1}{2}u_1-\frac{1}{3}u_2-u_3-\frac{2}{3}u_4\right)\\ -\frac{1}{3}\left(\frac{1}{2}u_2+u_4\right)-\mathrm{i}\frac{\sqrt{3}}{6}u_2\end{pmatrix}\qquad\text{and}\qquad U=(u_1,u_2,u_3,u_4)^{\mathrm{T}}.$$

In these coordinates, the linear part of (3.48) becomes at $\lambda=0$,

$$\begin{aligned}\partial_\tau\widetilde{A}&=\left(-\frac{1}{2}-\frac{\alpha}{2}+\mathrm{i}\left[\frac{\sqrt{3}}{2}-\frac{\alpha\sqrt{3}}{6}\right]\right)\widetilde{A}+\left(1+\frac{\alpha}{3}\right)\widetilde{B}+\alpha\left(\frac{1}{2}-\frac{\alpha\sqrt{3}}{6}\right)\overline{\widetilde{A}}-\frac{\alpha}{3}\overline{\widetilde{B}},\\ \partial_\tau\widetilde{B}&=\left(-\frac{1}{2}-\frac{\alpha}{2}+\mathrm{i}\left[\frac{\sqrt{3}}{2}-\frac{\alpha\sqrt{3}}{6}\right]\right)\widetilde{B}+\alpha\left(-\frac{1}{2}+\frac{\alpha\sqrt{3}}{6}\right)\overline{\widetilde{B}},\\ \partial_\tau\alpha&=-\alpha(2+\alpha).\end{aligned}\tag{3.49}$$

We can find a similar transformation to (3.12) for the Euclidean case, given in lemma 3.5.

**Lemma 3.5.** *Fix $0<m<\infty$, then there exists a change of coordinates*

$$\begin{pmatrix}A\\ B\end{pmatrix}=\mathrm{e}^{-\mathrm{i}\phi(r)}[1+\mathcal{T}(\alpha)]\begin{pmatrix}\widetilde{A}\\ \widetilde{B}\end{pmatrix}+O((|\lambda|+|\widetilde{A}|+|\widetilde{B}|)(|\widetilde{A}|+|\widetilde{B}|)),\tag{3.50}$$

*so that (3.49) becomes*

$$\begin{aligned}\partial_\tau A&=\left(-\frac{1}{2}-\frac{\alpha}{2}\right)A+B+\text{h.o.t.},\\ \partial_\tau B&=\left(-\frac{1}{2}-\frac{\alpha}{2}\right)B+c_1\lambda A+\text{h.o.t.},\\ \partial_\tau\alpha&=-\alpha(2+\alpha).\end{aligned}\tag{3.51}$$

*The constant $c_1$ is given by*

$$c_1=-s_1\frac{\Gamma_1+\Gamma_2}{3}$$

*The coordinate change is polynomial in $(A,B,\alpha)$ and smooth in $\lambda$ and $\mathcal{T}(\alpha)=O(\alpha)$ is linear and upper triangular for each $\alpha$, while $\phi(r)$ satisfies*

$$\partial_r\phi(r)=\frac{\sqrt{3}}{2}+O(|\lambda|+|\alpha|+|A|^2),\quad \phi(0)=0.$$

Note that at $(\alpha, \lambda) = (0, 0)$, the trivial state $(A, B) = (0, 0)$ is hyperbolic such that the higher order terms in equation (3.51) are exponentially small for $\tau \gg 1$ and $\lambda$ small enough and can be neglected. We can also directly solve the linear part of equation (3.51) to obtain

$$\begin{pmatrix} A(\tau) \\ B(\tau) \end{pmatrix} = \frac{1}{\sqrt{\sinh(\tau)}} \left[ q_1 \mathrm{e}^{-\tau\sqrt{c_1\lambda}} \begin{pmatrix} 1 \\ -\sqrt{c_1\lambda} \end{pmatrix} + q_2 \mathrm{e}^{\tau\sqrt{c_1\lambda}} \begin{pmatrix} 1 \\ \sqrt{c_1\lambda} \end{pmatrix} \right]. \tag{3.52}$$

We want to find solutions that have a finite energy density with respect to the hyperbolic measure, i.e. functions that are in $\mathrm{L}^2(\mathbb{R}^+, \sinh(\tau)\,\mathrm{d}\tau)$. This restriction implies that we need to track the stable fast manifold $\mathcal{W}^{\mathrm{sf}}_+(\lambda)$ of equation (3.52) which corresponds to eigenvalues $\ell$ of $\mathcal{A}(\infty, \lambda)$ with real part less than $-\frac{1}{2}$ as shown in figure 2. Thus, for each fixed $\tau_0 \gg 1$ and for all sufficiently small $\lambda < 0$, we can write the $\tau = \tau_0$-fiber of the stable fast manifold $\mathcal{W}^{\mathrm{sf}}_+(\lambda)$ of equation (3.52) near $U = 0$ as

$$\mathcal{W}^{\mathrm{sf}}_+(\lambda)\,|_{\tau=\tau_0} \;:\; \begin{pmatrix} A \\ B \end{pmatrix} = \mathrm{e}^{-\tau_0/2} \left[ -\eta\sqrt{c_1\lambda}\left(1 + O_{\tau_0}(|\lambda|)\right) \begin{pmatrix} \tau_0 \\ 1 \end{pmatrix} + \sqrt{c_1\lambda}\eta \begin{pmatrix} 1 \\ 0 \end{pmatrix} \right], \tag{3.53}$$

for $\eta \in \mathbb{C}$.

We can now finish the proof of theorem 2.2. To do this, we need to find non-trivial intersections of the stable fast manifold $\mathcal{W}^{\mathrm{sf}}_+(\lambda)$ with the centre-unstable manifold $\mathcal{W}^{\mathrm{cu}}_-(\lambda)$. To this end, we write the expansion (3.46) for each fixed $\tau_0 \gg 1$ in the $(\tilde{A}, \tilde{B})$ coordinates and afterwards in the coordinates $(A, B)$. Using the expansions of the associated Legendre functions given in table 1 we arrive at the expression

$$\begin{aligned} \begin{pmatrix} \tilde{A} \\ \tilde{B} \end{pmatrix} = \mathrm{e}^{-\tau_0/2} \Bigg[ & \mathrm{e}^{\mathrm{i}\left(\frac{\sqrt{3}}{2}\tau_0 + \Phi_0\right)} \begin{pmatrix} \frac{C_0}{2}\tilde{d}_1(1 + O(1)) + \tau_0\tilde{d}_2\left(-\mathrm{i}\frac{\sqrt{3}C_0}{6} + O(1)\right) \\ -\tilde{d}_2(\mathrm{i}\frac{\sqrt{3}C_0}{6} + O(1)) + \frac{C_1\sqrt{3}}{6}\left(\Xi_{\tilde{d}_1^2}\tilde{d}_1^2 + \Xi_{\tilde{d}_1\tilde{d}_2}\tilde{d}_1\tilde{d}_2\right) \end{pmatrix} \\ & + \mathrm{e}^{\mathrm{i}\left(\frac{\sqrt{3}}{2}\tau_0 + \Phi_0\right)} \begin{pmatrix} O_{\tau_0}(\lambda|\tilde{d}| + |\tilde{d}|^2) \\ O_{\tau_0}(\lambda|\tilde{d}| + |\tilde{d}_2|^2 + |\tilde{d}_1|^3) \end{pmatrix} \Bigg]. \end{aligned} \tag{3.54}$$

We can apply the transformation (3.50) to equation (3.54) and obtain the expansion

$$\begin{aligned} \mathcal{W}^{\mathrm{cu}}_-(\lambda)\,|_{\tau=\tau_0} \;:\; \begin{pmatrix} A \\ B \end{pmatrix} = & \mathrm{e}^{\mathrm{i}(\Phi_0 + O(\tau_0^{-2}) + O_{\tau_0}(\lambda|\tilde{d}| + |\tilde{d}|^2))} \begin{pmatrix} O_{\tau_0}(\lambda|\tilde{d}| + |\tilde{d}|^2) \\ O_{\tau_0}(\lambda|\tilde{d}| + |\tilde{d}_2|^2 + |\tilde{d}_1|^3) \end{pmatrix} \\ & + \mathrm{e}^{\mathrm{i}(\Phi_0 + O(\tau_0^{-2}) + O_{\tau_0}(\lambda|\tilde{d}| + |\tilde{d}|^2))} \begin{pmatrix} \frac{C_0}{2}\tilde{d}_1(1 + O(1)) + \tau_0\tilde{d}_2(-\mathrm{i}\frac{\sqrt{3}C_0}{6} + O(1)) \\ -\tilde{d}_2(\mathrm{i}\frac{\sqrt{3}C_0}{6} + O(1)) \end{pmatrix} \\ & + \mathrm{e}^{\mathrm{i}(\Phi_0 + O(\tau_0^{-2}) + O_{\tau_0}(\lambda|\tilde{d}| + |\tilde{d}|^2))} \begin{pmatrix} 0 \\ \frac{C_1\sqrt{3}}{6}\left(\Xi_{\tilde{d}_1^2}\tilde{d}_1^2 + \Xi_{\tilde{d}_1\tilde{d}_2}\tilde{d}_1\tilde{d}_2\right) \end{pmatrix}. \end{aligned} \tag{3.55}$$

As in the Euclidean case, the final step of the analysis consists in finding non-trivial intersections of the stable fast manifold $\mathcal{W}^{\mathrm{sf}}_+(\lambda)$ given above in equation (3.53) and the core manifold $\mathcal{W}^{\mathrm{cu}}_-(\lambda)$ given in (3.55). We can easily solve this problem in $(\tilde{d}_1, \tilde{d}_2)$ to find that

$$\tilde{d}_1 = -\frac{C_0}{C_1\,\Xi_{\tilde{d}_1^2}}\sqrt{3\lambda c_1}, \qquad \text{and} \qquad \tilde{d}_2 = O(\lambda).$$

This completes the proof of theorem 2.2.

## 4. Numerical analysis

In this section, we describe the use of numerical continuation (and the continuation package AUTO07p [37]) to compute solutions of the systems of ODEs described by (3.7) in the Euclidean

case and (3.39) in the hyperbolic case. Solutions of these spatial dynamical systems correspond to steady states of the neural field equation (2.1) where the radial coordinate $r$ in the Euclidean case or the geodesic polar radial coordinate $\tau$ in the hyperolic case has been recast as time in AUTO07P's boundary value problem (BVP) solver. The BVP is set up on the domain $r \in [0, L]$ (or $\tau \in [0, L]$) with homogeneous Neumann boundary conditions given by $u_2(0) = u_4(0) = u_1(L) = u_3(L) = 0$. Typical parameters for the AUTO07P radial computations are $L = 1000$ and AUTO07P's NTST=400 with standard relative tolerances that are specified in AUTO07P's manual. In order to compute initial solutions to start AUTO07P computations and to compute solutions that are not radially symmetric, we solve equation (3.6) in the Euclidean case and (3.38) in the hyperbolic case in polar coordinates where we discretise in the radial variable with finite-differences and a pseudo-spectral Fourier method in the angular variable; see Avitabile *et al* [9]. The resulting discretization is then solved in Matlab using the FSOLVE routine with a Levenberg-Marquardt algorithm, the Jacobian implemented and standard tolerances. For $\boldsymbol{D}_6$-symmetric solution branches in the Euclidean case and $\boldsymbol{D}_8$-symmetric solution branches in the Hyperbolic case FSOLVE was used in conjunction with standard secant continuation method [71]. For the full 2D computations, we compute on the positive quadrant and take the radial truncation to be $L = 60$ with 500 finite-difference points and 20 Fourier modes in the angular direction.

### *4.1. Tuning the parameters*

Before numerically studying stationary localized radial solutions on the two geometries, we first reduce the set of parameters governing the shape of the connectivity function and the firing rate function. In both geometries, the connectivity function $W$, defined in equations (2.3) and (2.19), depends upon the same set of parameters $(b_1, b_2, \sigma_1, \sigma_2)$ and satisfies equivalent hypotheses 2.1 and 2.2, respectively. Note that the sigmoidal function, defined in equation (2.2), depends upon two parameters $(\mu, \theta)$. Based on the study conducted by Faye *et al* [46] on the real line, we fix the value of the threshold to $\theta = 3.5$.

Following the same lines as in [46], space can be rescaled such that, without loss of generality, $\sigma_1 = 1$. The important quantities for the connectivity function are $\widehat{W}_0$, $\widehat{W}_c$ (respectively $\widetilde{W}_0$, $\widetilde{W}_c$), which determine the overall shape of the Hankel transform (respectively Mehler–Fock transform) of $W$. The connectivity function can then be reparametrized in terms of $(\widehat{W}_0, \widehat{W}_c)$ (respectively $(\widetilde{W}_0, \widetilde{W}_c)$) solely by the the parameters:

$$\sigma_2 = \sqrt{\frac{\widehat{W}_c}{\widehat{W}_c - \widehat{W}_0}},$$

$$b_1 = -\frac{2\widehat{W}_c(\widehat{W}_c - \widehat{W}_0)}{\widehat{W}_0},$$

$$b_2 = -\frac{(2\widehat{W}_c - \widehat{W}_0)^2}{2\widehat{W}_0}\sqrt{\frac{\widehat{W}_c}{\widehat{W}_c - \widehat{W}_0}}.$$

Finally, in order to express the connectivity function in terms of a single parameter, we fix $\widehat{W}_0 = -1$. Recall that $\widehat{W}_0$ has to be negative in order to ensure the existence of a unique trivial solution $v = 0$ of equation (2.1). Hence, the connectivity function only depends upon $\widehat{W}_c$ (respectively $\widetilde{W}_c$).

### *4.2. Numerical computation of the stability of localized solutions*

In the Euclidean case, in order to numerically investigate the radial stability of a stationary localized bump solution $V_0(r)$ of equation (2.1), we have to solve the following eigenvalue problem. We linearize equation (2.1) around $V_0(r)$ to find the linearized equation

$$\partial_t v(\boldsymbol{r}, t) = -v(\boldsymbol{r}, t) + \mu \int_{\mathbb{R}^2} W(\|\boldsymbol{r} - \boldsymbol{r}'\|) S'(\mu V_0(\|\boldsymbol{r}'\|)) v(\boldsymbol{r}', t)\, \mathrm{d}\boldsymbol{r}'. \tag{4.1}$$

Looking for radial perturbation of the form $v(\boldsymbol{r}, t) = \mathrm{e}^{\sigma t} q(r)$ and applying the PDE method developed in section 3.1.2 to equation (4.1), we obtain

$$(\sigma + 1)\mathcal{L}_0\,(q\,(r)) = \mu\,(\Gamma_1 - \Gamma_2 \Delta_r)\left[S'(\mu V_0\,(r)\, q\,(r)\right]. \tag{4.2}$$

The linear operator $\mathcal{L}_0$ is given by $\mathcal{L}_0 = \Delta_r^2 - (\sigma_1^2 + \sigma_2^2)\Delta_r + \sigma_1^2\sigma_2^2$. For all $q \in \mathcal{H}^4(\mathbb{R}_*^+) = \{u \in \mathrm{L}^2(\mathbb{R}_*^+) \mid \forall k \leqslant 4\ \partial_{r^k}^k u\,(r) \in \mathrm{L}^2(\mathbb{R}_*^+)\}$ and $p \in \mathrm{L}^2(\mathbb{R}_*^+)$, we set $\mathcal{L}_0 q = p$. As the spectrum of $\mathcal{L}_0$ is given by $\mathrm{spec}_{\mathcal{L}_0} = \{\rho^4 + (\sigma_1^2 + \sigma_2^2)\rho^2 + \sigma_1^2\sigma_2^2 \mid \rho \in \mathbb{R}\} \subset [\sigma_1^2\sigma_2^2, +\infty[$, $\mathcal{L}_0$ is an invertible operator and $q = \mathcal{L}_0^{-1} p$. It follows that equation (4.2) can be rewritten:

$$\sigma p\,(r) = -p\,(r) + \mu\,(\Gamma_1 - \Gamma_2\Delta_r)\left[S'(\mu V_0\,(r))\mathcal{L}_0^{-1} p\,(r)\right] = \mathcal{B}(p\,(r)). \tag{4.3}$$

Now, for every solution $V_0$ discretized on a domain $[0, L]$, we compute the eigenvalues $\sigma$ of the corresponding discretized version of the linear operator $\mathcal{B}$ where we use finite difference methods to approximate the Laplacian operator $\Delta_r$. The results in [89] imply that spectral stability also implies linear (asymptotic) stability. Hence, when all the eigenvalues of $\mathcal{B}$ have negative real part, we say the solution is radially stable and unstable otherwise.

The radial stability in the hyperbolic case is computed in a similar fashion. If $V_0(\tau)$ is a stationary localized bump solution of equation (2.11) then the linearized equation around $V_0(\tau)$ is:

$$\partial_t v(z, t) = -v(z, t) + \mu \int_{\mathbb{D}} W(d_{\mathbb{D}}(z, z')) S'(\mu V_0(d_{\mathbb{D}}(z', 0))) v(z', t) \mathrm{dm}(z'). \tag{4.4}$$

Looking for radial perturbation of the form $v(z, t) = \mathrm{e}^{\sigma t} q(\tau)$ and applying the PDE method developed in section 3.2.2 to equation (4.4), we obtain:

$$(\sigma + 1)\mathcal{L}_0^{\mathbb{D}}\,(q\,(\tau)) = \mu\left(\Gamma_1 - \Gamma_2 L_{\mathbb{D}}^{\tau}\right)\left[S'(\mu V_0\,(\tau)\, q\,(\tau)\right]. \tag{4.5}$$

$L_{\mathbb{D}}^{\tau}$ is defined in equation (2.16) and the linear operator $\mathcal{L}_0^{\mathbb{D}}$ is given by $\mathcal{L}_0 = \left(L_{\mathbb{D}}^{\tau}\right)^2 - (\sigma_1^2 + \sigma_2^2)L_{\mathbb{D}}^{\tau} + \sigma_1^2\sigma_2^2$ is aslo invertible, as its spectrum is positive. If we denote $q = \left(\mathcal{L}_0^{\mathbb{D}}\right)^{-1} p$. It follows that equation (4.5) can be rewritten:

$$\sigma p\,(\tau) = -p\,(\tau) + \mu\left(\Gamma_1 - \Gamma_2 L_{\mathbb{D}}^{\tau}\right)\left[S'(\mu V_0\,(\tau))\left(\mathcal{L}_0^{\mathbb{D}}\right)^{-1} p\,(\tau)\right] = \mathcal{B}^{\mathbb{D}}(p\,(\tau)). \tag{4.6}$$

Again, for every solution $V_0$ discretized on a domain $[0, L]$, we compute the eigenvalues $\sigma$ of the corresponding discretized version of the linear operator $\mathcal{B}^{\mathbb{D}}$ where we use finite difference methods to approximate the Laplace–Beltrami operator $L_{\mathbb{D}}^{\tau}$. When all eigenvalues have negative real part, then the solution is said to be radially stable, otherwise it is unstable.

We note that stability with respect to other perturbations (in particular $\boldsymbol{D}_n$-perturbations) can similarly be investigated by carrying out a polar discretization of the differentiation operators in $\mathcal{B}$ and $\mathcal{B}^{\mathbb{D}}$ as described above.

### *4.3. Euclidean case*

*4.3.1. Radially symmetric solution branches.* We present branches of radial solutions on the Euclidean plane for the reduced system of ODEs given in (3.7). In this section, we fix

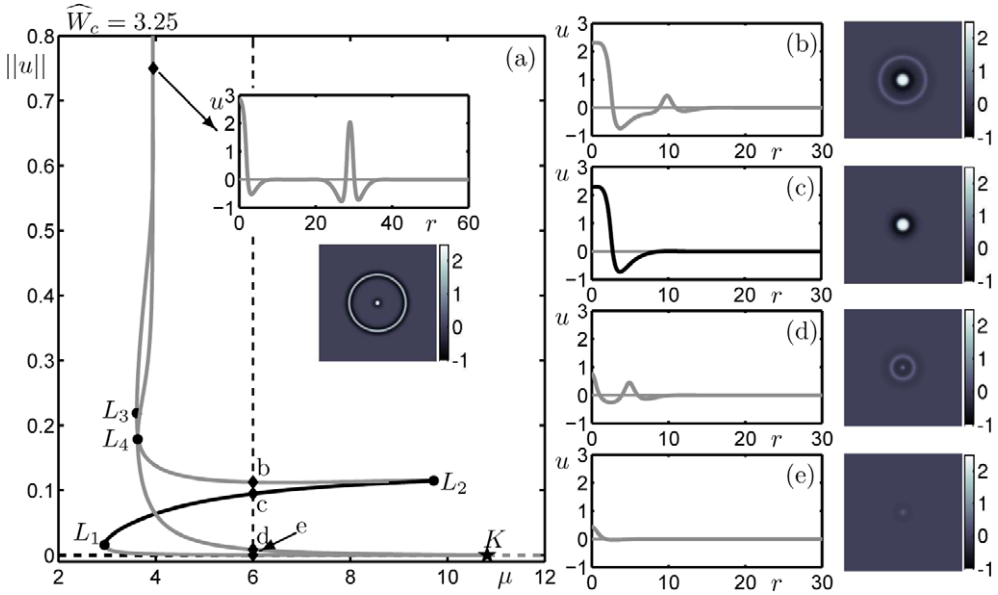


**Figure 3.** Radial solutions in the Euclidean case. (*a*) Bifurcation diagram in $\mu$ where stable solution branch segments are black and unstable segments are grey. The trivial solution branch at $\|u\|_{L^2} = 0$ is dashed and the two branches bifurcating at the Turing instability $K$ are solid. The first branch undergoes three fold bifurcations $L_1$, $L_2$ and $L_3$ and is stable between $L_1$ and $L_2$; the second branch undergoes a fold at $L_4$; both branches asymptote at $\mu = 3.94$. The inset shows the solution profiles on the asymptote. (*b*) Solution profiles at $\mu = 6$ (vertical dashed line) on the branch segment between $L_2$ and $L_3$. (*c*) Solution profiles at $\mu = 6$ on the branch segment between $L_1$ and $L_2$. (*d*) Solution profiles at $\mu = 6$ on the branch segment between $K$ and $L_4$. (*d*) Solution profiles at $\mu = 6$ on the branch segment between $K$ and $L_1$. Each solution profile is visualized through a 1D slice (left) and a pseudocolor plot in the Euclidean plane (right).

the critical Fourier mode $\widehat{W}_c = 3.25$ that fixes the critical value of the sigmoidal slope to $\mu_c = 10.81$ (given by (3.3)) for which there is a Turing instability for the trivial state $u_1 = 0$. Figure 3(*a*) shows a bifurcation diagram value $\mu$ where the solution branches are represented in terms of the $L^2$-norm $\|u\|_{L^2} = (\int_0^\infty u(r)^2 r \mathrm{d}r)^{1/2}$. The inset 3(*a*) and panels 3(*b*)–(*e*) show solution profiles at different points on the bifurcation diagram as indicated. Two branches of spatially localized solutions bifurcate from the trivial state at the bifurcation point $K$ where $\mu = \mu_c$. The first branch represents a bump solution, as shown in panel (*e*) for $\mu = 6$, on the segment between $K$ and $L_1$ and this solution is initially unstable. The branch becomes stable and the bump solution becomes a spot solution, as shown in panel (*c*) for $\mu = 6$, at the fold bifurcation $L_1$. The branch loses stability and a ring is added to the spot, as shown in panel (*b*) for $\mu = 6$, at the fold point $L_2$. After a further fold point $L_3$ the ring starts to travel away from the core, as shown in the inset of (*a*), and the solution branch asymptotes at $\mu = 3.94$ in a gluing bifurcation. Such glueing bifurcations involving radial spots have been observed in other reaction–diffusion systems [10] (though it is an open problem to explain why the bifurcation is co-dimension one as the pulse in the $r = \infty$ invariant subspace is co-dimension zero). The second branch represents an unstable bump solution with a ring and in a similar fashion the branch asymptotes in a gluing bifurcation where the ring travels away from the core.

So far, we have identified a particular range of $\mu$ for which localized radial solutions exist, for specific values of the critical Fourier mode $\widehat{W}_c = 3.25$. We now show that localized bump

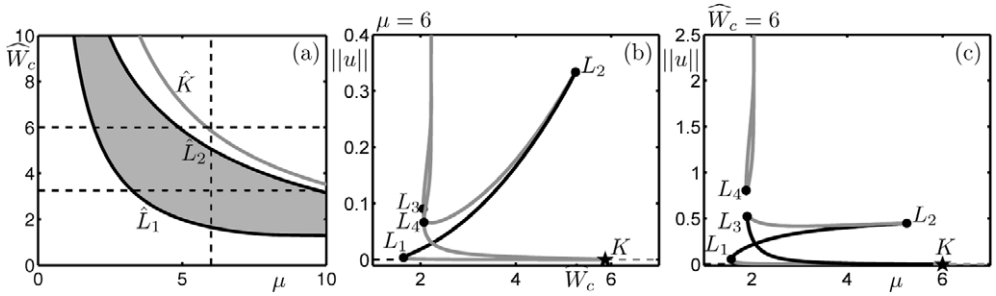


**Figure 4.** Two-parameter solution structure in the Euclidean case. (*a*) Two parameters bifurcation diagram in the $(\mu, \widehat{W}_c)$-plane. The locus $\widehat{K}$ of the bifurcation point $K$ shown in figure 3(*a*) is grey; the loci $\widehat{L}_1$ and $\widehat{L}_2$ of the respective fold points $L_1$ and $L_2$ are black. A stable spot solution, as shown in figure 3(*c*), persists in the region between $\widehat{L}_1$ and $\widehat{L}_2$, which is shaded in grey. Dashed lines are the one-dimensional slices corresponding to the one-parameter diagrams shown in figure 3(*a*) and panels (*b*) and (*c*). (*b*) One-parameter diagram in $\widehat{W}_c$ at $\mu = 6$. (*c*) One-parameter diagram in $\mu$ at $\widehat{W}_c = 6$.

solutions persist over a range of the parameters $(\mu, \widehat{W}_c)$ and are not an isolated phenomena in parameter space. First we observe that, as shown in figure 3(*a*), the branch of localized bump solutions is stable with respect to radial perturbations between the two fold points $L_1$ and $L_2$ for all the associated $\mu$-values as as indicated by the black curve. Therefore, assuming that this is also the case when $\widehat{W}_c$ is varied, we can find bounds of regions for which localized bump solutions exist; in the $(\mu, \widehat{W}_c)$-plane it is sufficient to track the loci of the fold points $L_1$ and $L_2$ under the simultaneous variation of those two parameters. We denote $\widehat{K}$ the locus of the bifurcation point $K$ shown in figure 3(*a*) and we denote $\widehat{L}_1$ and $\widehat{L}_2$ the loci of the respective fold points $L_1$ and $L_2$.

Figure 4(*a*) shows curves that are the loci of bifurcations in the $(\mu, \widehat{W}_c)$ parameter plane. The curve $\widehat{K}$ is the locus of the Turing bifurcation at $\mu_c$, which is determined analytically by the expression $\mu_c = 1/(s_1 \widehat{W}_c)$. The curves $\widehat{L}_1$ and $\widehat{L}_2$ bound the region for which localized bump solutions persist (shaded in grey). Under the variation of $\mu$ and $\widehat{W}_c$, shown in figure 4(*a*), there is a channel in parameter space for which localized solutions exist. The vertical line in figure 4(*a*) corresponds to the default value $\mu = 6$ and the corresponding bifurcation diagram as $\widehat{W}_c$ is varied is shown in figure 4(*b*). We note that this bifurcation diagram has the same characteristics as the one obtained when varying $\mu$ (see figure 3(*a*)) with $\widehat{W}_c = 3.25$. We also remark that in both cases the localized bump solutions always exist before the Turing bifurcation. Therefore, the localized bump solutions coexist with a stable trivial solution. One horizontal line in figure 4(*a*) corresponds to the default value of $\widehat{W}_c$ used in figure 3 and the other one at $\widehat{W}_c = 6$ is shown in figure 4(*c*). The bifurcation diagram in figure 4(*c*) shows that the folds $L_3$ and $L_4$ have undergone a saddle transition creating two separate branches, one connected back to $K$ and one that asymptotes at $\mu = 2.10$. Similar saddle transition scenario has been encountered in [9] for branches of fully localized stripe patterns (worms) in the planar Swift–Hohenberg equation with cubic/quintic nonlinearity; see [9].

*4.3.2. $\boldsymbol{D}_6$-symmetric solution branch.* In order to detect possible bifurcations from the radial solution branch to non-radially symmetric solutions, the radial ODE system is augmented with the linearized system with respect to $\boldsymbol{D}_6$ perturbations; see [78]. We concentrate on $\boldsymbol{D}_6$-perturbations since hexagons are usually the most stable patterns in Euclidean geometry due to close-packing arguments. Note that a symmetry breaking to $\boldsymbol{D}_6$-symmetric solutions has

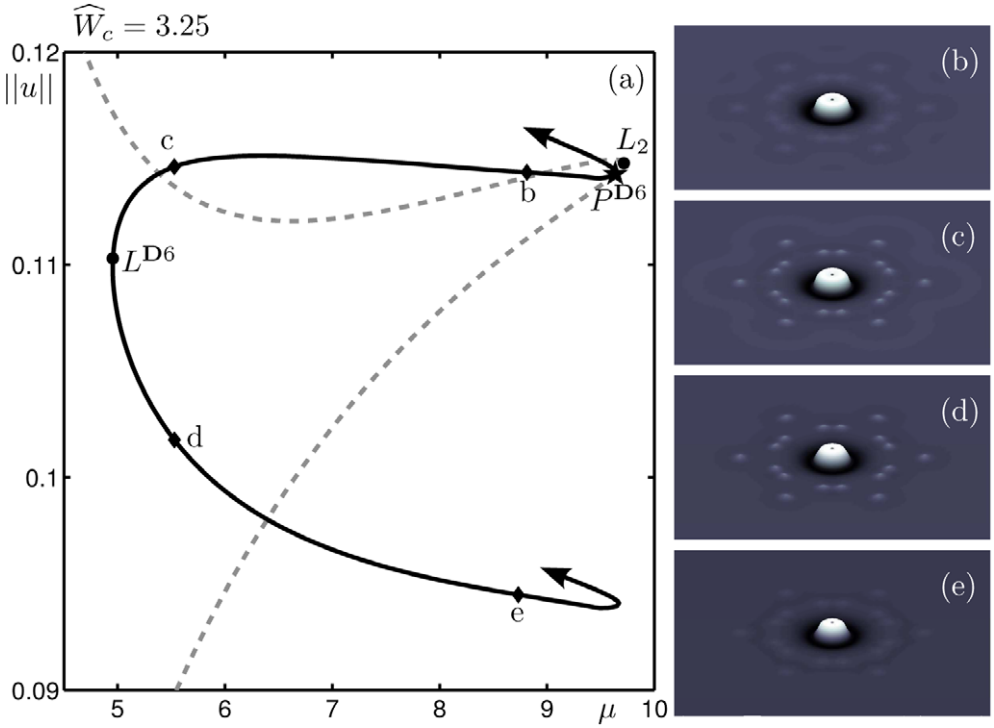


**Figure 5.** $D_6$-symmetric solutions in the Euclidean case. (*a*) Zoom of figure 3(*a*) close to $L_2$ with a branch segment of $D_6$-symmetric solutions plotted. The $D_6$-branch bifurcates from the radially stable branch at $P^{D_6}$, close to $L_2$; the $D_6$-branch undergoes a fold bifurcation at $L^{D_6}$ and further fold bifurcations at a $\mu$-value slightly smaller than that of $L_2$. Further branch segments that are not shown are indicated by arrows. (*b*)–(*e*) Solution profiles from different points on the $D_6$-branch plotted in the euclidean plane.

already been observed in several previous neural field studies, some of them using a sigmoidal function firing rate function [50, 72, 85]. Figure 5 shows detail of figure 3(*a*) near the fold point $L_1$ and a possible bifurcation to a $D_6$-symmetric branch was detected in AUTO07p at the point $P^{D_6}$ (note that when traced in the $(\mu, \widehat{W}_c)$-plane, the point $P^{D_6}$ was found to follow $L_1$ very closely). In order to find a solution on the $D_6$-branch it was necessary to reconverge the solution from the bifurcation point in Matlab and confirm that there is locally a zero-crossing of an eigenvalue $\sigma$ associated with an eigenfunction $q$ of (4.2) that is $D_6$-symmetric. Note that $\sigma$ and $q$ are computed numerically from the Jacobian at the equilibrium point. Using the eigenfunction as a perturbation at a parameter value of $\mu$ less than at $P^{D_6}$ we are able to converge a solution on the $D_6$-symmetric branch. A standard secant continuation method is then used to compute the new branch.

Figure 5 shows the branch of $D_6$-symmetric solutions that bifurcates off the original radial branch at $P^{D_6}$. The $D_6$-branch undergoes a fold bifurcation at $L^{D_6}$ and further fold bifurcations at a $\mu$-value slightly smaller than that of $L_2$. We see that as $\mu$ decreases, an inner ring of 12 cells and a outer ring of 6 cells with small amplitude is glued to the initial bump solution. The amplitude of these cells is largest as $L^{D_6}$ is approached. For the branch shown the numerical accuracy was tested by recomputing it with double the number of angular mesh points. The branches carry on as indicated by the arrows in figure 5 but they undergo a complicated sequence of folds that we leave for further study.

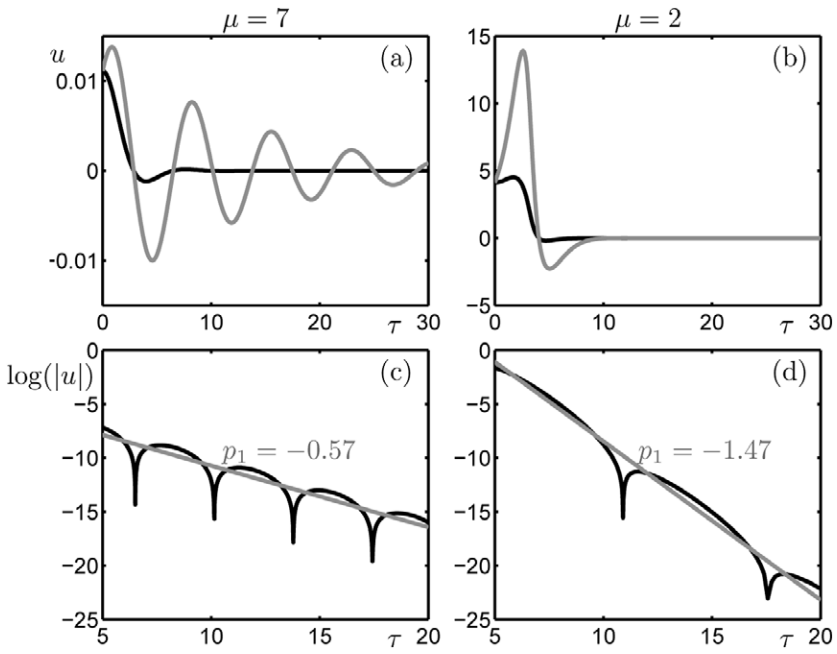


**Figure 6.** Decay rates of radial solutions in hyperbolic case. In panels (*a*) and (*b*) respectively, the solutions $u(\tau)$ at $\mu = 7$ and $\mu = 2$ are black and the same solutions rescaled as $u(\tau)e^{\tau/2}$ are grey. Panels (*c*) and (*d*) show the decay rate of the tails of the solutions in black at $\mu = 7$ and $\mu = 2$, respectively. Linear best fits are shown in grey with the linear coefficients $p_1$ as indicated.

### *4.4. Hyperbolic radial case*

Before tracing out the bifurcation diagrams for the radial spots, we verify that the spots found in theorem 2.2 are $L^2(\mathbb{R}^+, \sinh(\tau)\,d\tau)$ functions. In figure 6, we show the radial states and the decay rate of their tails. Figures 6(*a*) and (*b*) show radial spot solutions $u(\tau)$ close to $\mu_c$ at $\mu = 7$ and on a connected radially stable branch segment at $\mu = 2$, respectively. In each case we also show the same solutions rescaled by $e^{\tau/2}$; these rescaled solutions still decay, which shows that in each case the decay is faster than $e^{-\tau/2}$ as predicted in section 3.2.4. Close to onset at $\mu = 7$, figure 6 shows that the bifurcating pulse has highly oscillatory tails as also predicted by the analysis. Plotting the decay rate of the tails of the radial states, figures 6(*c*) and (*d*) confirm that for $\mu = 7$ and $\mu = 2$, both states decay faster than $e^{-\tau/2}$ and hence are in $L^2(\mathbb{R}^+, \sinh(\tau)\,d\tau)$. In particular, we see in figure 6(*c*), that close to onset the decay rate converges to a half as predicted.

We now present branches of radial solutions on the Poincaré disc for the reduced system of ODEs given in (3.39). In figure 7(*a*), we fix the critical Fourier mode $\widetilde{W}_c = 5$ that fixes the critical value of the sigmoidal slope to $\mu_c = 7.03$ (given by (3.35)). Figure 7(*a*) shows a bifurcation diagram in $\mu$ where the solution branches are represented in terms of the Euclidean $L^2$-norm $\|u\|_{L^2} = (\int_0^\infty u(\tau)^2\tau\,d\tau)^{1/2}$. This is due to numerical difficulties of computing the hyperbolic $L^2$ norm presented by the sinh-function in the integrand but we believe the Euclidean radial norm to be a good solution measure. The panels (*c*)–(*f*) show solution profiles at different points on the bifurcation diagram as indicated. The branch represents a bump solution, as shown in panel (*f*) for $\mu = 2$, on the segment between $K$ and $L_1$ and this solution is initially unstable ($K$ is only shown in figure 7(*b*)). The branch becomes stable and

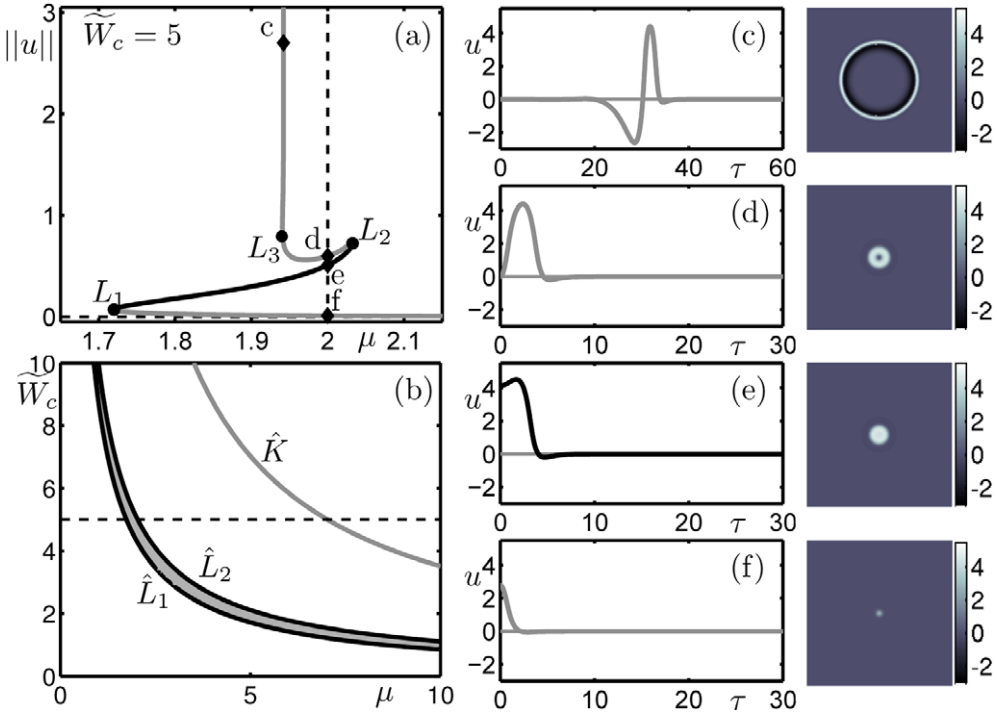


**Figure 7.** Radial solutions in the hyperbolic case. (*a*) One-parameter bifurcation diagram in $\mu$ at $\widetilde{W}_c = 5$. A single solution branch originating from $K$ (not shown) has a stable segment between $L_1$ and $L_2$ and asymptotes at $\mu = 1.95$. (*c*) Solution profiles on the asymptote. (*d*) Solution profiles at $\mu = 2$ on the branch segment between $L_2$ and the asymptote. (*e*) Solution profiles at $\mu = 2$ on the branch segment between $L_1$ and $L_2$. (*f*) Solution profiles at $\mu = 2$ on the branch segment between $K$ and $L_1$. Each solution is visualized through a 1D slice (left) and a pseudocolor plot in polar geodesic coordinates (right).

the bump solution becomes a spot solution at the fold bifurcation $L_1$; see panel (*e*) for $\mu = 2$. The branch loses stability and the spot decays at the core at the fold point $L_2$; see panel (*d*) for $\mu = 2$. After a further fold point $L_3$ the spot starts to travel away from the core, as shown in the inset of (*c*), and the solution branch asymptotes at $\mu = 1.95$.

We denote $\widehat{K}$ the locus of the bifurcation point $K$ and we denote $\widehat{L}_1$ and $\widehat{L}_2$ the loci of the respective fold points $L_1$ and $L_2$. Figure 7(*b*) show curves that are the loci of bifurcations in the $(\mu, \widetilde{W}_c)$ parameter plane. The curve $\widehat{K}$ is the locus of the Turing bifurcation at $\mu_c$, which is determined analytically by the expression $\mu_c = 1/(s_1 \widetilde{W}_c)$. The curves $\widehat{L}_1$ and $\widehat{L}_2$ bound the region for which localized bump solutions persist (shaded in grey). Under the variation of $\mu$ and $\widetilde{W}_c$, shown in figure 7(*b*), there is a channel in parameter space for which localized solutions exist. The horizontal line in figure 7(*b*) corresponds to the default value of $\widetilde{W}_c$ used in figure 7(*a*). We can see that the region for which localized bump solutions persist is much thinner in the hyperbolic case than in the Euclidean case. This implies that radial stationary spots are more likely to be seen in the Euclidean plane than in the Poincaré disc. Furthermore, the bifurcation where the asymptote occurs, is fundamentally different. In the Euclidean case, the asymptote is due to a glueing bifurcation between a bump solution at the core and a symmetric pulse in the $r = \infty$ invariant subspace. In the Hyperbolic case, the bifurcation is due to the fact that there is co-dimension one homoclinic bifurcation where an

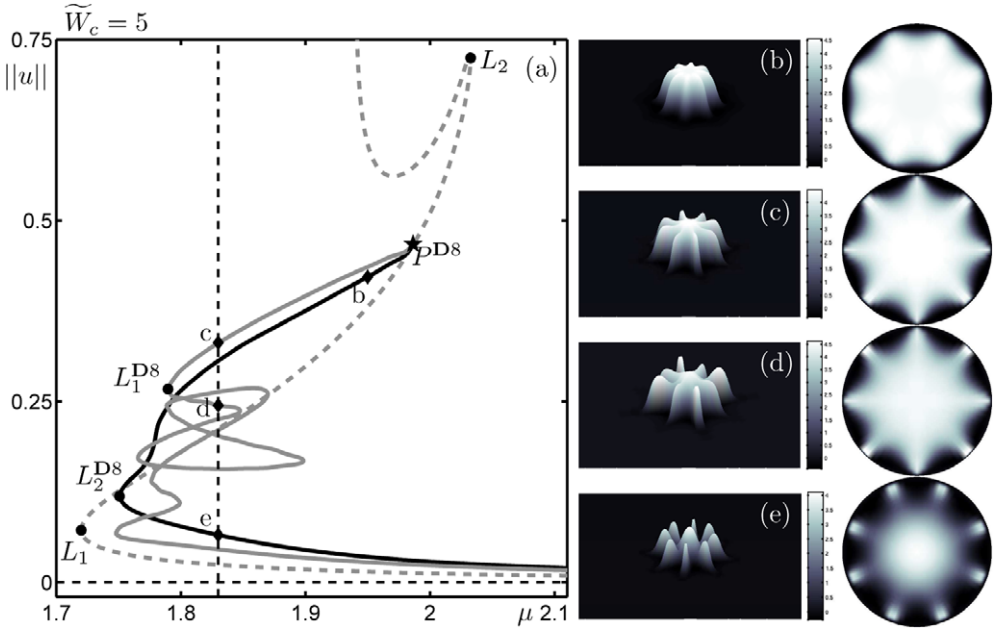


**Figure 8.** $\boldsymbol{D}_8$-symmetric solutions in the Hyperbolic case. (*a*) Zoom of figure 7(*a*) where radial solution branches are now dashed grey. Two new branches of $\boldsymbol{D}_8$-symmetric solutions bifurcate from the radial branch between $L_1$ and $L_2$ at $P^{D8}$. The upper segment is grey and undergoes a fold bifurcation $L_1^{D8}$ followed by a series of unlabelled fold bifurcations. The lower segment is black and undergoes a single fold bifurcation $L_2^{D8}$. Panels (*b*)–(*e*) show solution profiles plotted in polar geodesic coordinates (left) and in the hyperbolic disc (right). Panels (*b*) and (*e*) are from the lower $\boldsymbol{D}_8$-branch at points above and below $L_2^{D8}$, respectively. Panels (*c*) and (*d*) are from upper branch at points above and below $L_1^{D8}$, respectively.

asymmetric pulse occurs in the $\tau = \infty$-invariant subspace. The reason why the bifurcation in the hyperbolic case is co-dimension one is due to the fact that in the $\tau = \infty$ invariant subspace, the stationary equations no longer have spatial reflectional symmetry, hence an odd pulse; since the ODE system is not conservative such pulses are generically co-dimension one.

*4.4.1. $\boldsymbol{D}_8$-symmetric solution branch.* In [27, 47], Chossat and Faye studied the bifurcations of periodic solutions in the Poincaré disc with octagonal symmetry for neural field equations similar to (2.11). They were able to, for each absolutely irreducible representation, classify all the corresponding isotropy subgroups satisfying the equivariant branching lemma [28, 53]; $\boldsymbol{D}_8$ appears naturally as such an isotropy subgroup [27]. Hence, it is natural to look for $\boldsymbol{D}_8$-symmetric localized solutions. Note, we have found that the radial spot undergoes other dihedral instabilities (in particular $\boldsymbol{D}_4$ and $\boldsymbol{D}_6$ instabilities) but we concentrate on the $\boldsymbol{D}_8$ instability.

With a similar approach as was taken in section 4.3.2, we find a branch of $\boldsymbol{D}_8$-symmetric solutions bifurcating from the main, stable, radial branch that was shown in figure 7(*a*). Figure 8(*a*) shows a zoom of figure 7 with a $\boldsymbol{D}_8$-symmetric branch of solutions that bifurcates from the radial branch at $P^{D_8}$. The bifurcated branch exists for $\mu$-values below $P^{D_8}$ and has an upper and a lower segment. The lower segment undergoes a single fold bifurcation at $L_2^{D_8}$ before reconnecting back to the trivial solution branch at the Turing instability $K$ (not shown in figure 8(*a*)). The upper branch undergoes a series of fold bifurcations starting with $L_1^{D_8}$

and also connects back to $K$. The solution profile on the lower branch close to $P^{D_8}$ in panel ($b$) shows a $\boldsymbol{D}_8$-symmetric spot solution. After the fold bifurcation $L_2^{D_8}$, one can see that the solution has formed a spot solution surrounded by a ring of 8 smaller cells; see panel ($e$). On the upper branch, there is also a $\boldsymbol{D}_8$-symmetric spot solution as shown in panel ($c$). After the fold bifurcation $L_1^{D_8}$ we see that the solution has 4 out of 8 nodes at an elevated activity level. For the $\boldsymbol{D}_6$ solution branches discussed in section 4.3.2, we found that at the bifurcation from the radial branch, a ring of cells was glued to the main radially symmetric solution. Here, in contrast, we find that a modified spot solution that is $\boldsymbol{D}_8$-symmetric; although a ring of 8 cells can also form about the spot as was shown in figure 8($e$).

## 5. Conclusion

In this paper, we investigated radially localized solutions of a neural field equation set on the Euclidean plane and on the Poincaré disc equipped with their corresponding natural metrics. Applying an appropriate integral transform in both geometries we were able to reduce the neural field equations to partial differential equations and look for stationary radially symmetric solutions. We applied the techniques from Scheel [90] and Lloyd and Sandstede [77] to prove the existence of a branch of bump solutions bifurcating near onset for both Euclidean and hyperbolic geometries. In the Poincaré disc, the analysis near the core manifold required significant changes compared with the approach used for the Euclidean case; in hyperbolic geometry it was necessary to developed a detailed knowledge of the asymptotics of the associated Legendre functions. It turns out that the main difference between the two geometries comes from the far field. At infinity, Bessel function $J_0(r)$ scales in term of the radial coordinate $r$ as $1/\sqrt{r}$ whereas the associated Legendre function $\mathcal{P}_\nu(\cosh(\tau))$, with $\nu = -\frac{1}{2}+\mathrm{i}\frac{\sqrt{3}}{2}$, scales in terms of the polar geodesic coordinate $\tau$ as $\mathrm{e}^{-\tau/2}$. Moreover, in the Euclidean case for the trivial state at infinity there is a Turing instability bifurcation. However, in the hyperbolic case, the trivial state is always asymptotically stable at infinity and this simplifies the resulting matching problem. Other localized radial states are also expected and the theory developed in [80, 82] can be applied to yield the existence of rings and another spot solution not investigated in this paper.

Numerical continuation was used to track branches of spot solutions away from onset and we implemented a method to compute their radial stability. We identified regions of parameter space where the spot solutions are radially stable for both geometries. We also found branches of localized $\boldsymbol{D}_6$ symmetric and $\boldsymbol{D}_8$-symmetric solutions bifurcating off the stable radial branches in the Euclidean and hyperbolic geometries, respectively. In terms of the radial spot solutions, the region of radial stability in the Euclidean case is significantly larger than in the hyperbolic case. Although the region of stability is smaller in the hyperbolic case, we expect to find other types of stable radially symmetric solution, for example, time-periodic localized states; see [26]. In [46], the 1D analogueue of the present model was studied and stationary localized structures were shown to undergo homoclinic snaking, however, this does not occur for both of the 2D geometries studied here. This appears to be due to the connectivity function creating almost spike-like multi-pulse localized states similar to that seen in Lloyd and O'Farrell [76] for a different PDE system and we believe this is due to the presence of a singular limit nearby in parameter space. For the connectivity function chosen in the Laing and Troy model [72], snaking-like behavior was found on the Euclidean plane for radial localized solutions, we expect that the localized hexagon patches that were found in their study could also undergo homoclinic snaking similar to that observed in the planar Swift–Hohenberg equation [78].

For the neural field model set on the Euclidean plane, radially localized solutions can be interpreted as spatially localized regions of high activity on the cortex. In particular, this type of solutions is of interest in modeling working memory: the ability to remember information over a time-scale of a few seconds. Indeed, some experiments on primates [29, 51, 83] reveal that there are spatially localized regions of neurons with elevated firing rates during the period that the animal is remembering some aspect of an object or event. In this paper, we have been able to prove the existence of such solutions. More precisely, we have demonstrated that there exists radially localized solutions which bifurcate off the trivial state using dynamical systems methods developed by Scheel [90] and Lloyd and Sandstede [77]. This result provides a better understanding of the formation of this type of solutions in planar neural field equations (though near onset such states are unstable) and is complementary to the constructive approach used in [50, 93, 98]. We also identified a region in the parameter plane (one parameter for the connectivity function and one parameter for the slope of the firing rate function) where these solutions are stable with respect to radial perturbations and certain periodic perturbations, which generalizes the results presented in [72, 85].

Our results show that a cortical network with local excitatory and inhibitory connections can spontaneously produce regions of localized high activity. Another interpretation of these regions of localized activity is related to the recent work of Chavane *et al* [25] where it was found, using voltage sensitive dye imaging in the cat primary visual cortex, that localized oriented inputs in the visual field produce localized regions of activity in the cortical feedforward imprint of the input. Suppose now that we add to equation (2.1) an external input of the form $\epsilon I_{\text{ext}}(\|\boldsymbol{r}\|)$ with $0 < \epsilon \ll 1$ where $I_{\text{ext}}$ is radially localized. This breaks the translational symmetry but preserves the reflectional and rotational symmetry. Then, for small enough $\epsilon$, we still expect to find radially localized solution with a high region of activity for $(\mu, \widehat{W}_c)$ in the grey region of figure 4($a$). This type of result is well known for the ring model of orientation [14, 58, 95] and for the one-dimensional version of equation (2.1) [46]. A more detailed study of the effects of localized external inputs in equation (2.1) will be the subject of future work. We have also demonstrated in the Euclidean case the existence of radially localized solutions with a ring of glued $\boldsymbol{D}_6$-symmetric patches that is another possible response to localized inputs. Indeed, such patchy localized responses have been experimentally recorded in the primary visual cortex [3, 79].

The neural field equation (2.11) set on the Poincaré disc has been used to model orientation and texture selectivity for a hypercolumn of the primary visual cortex [26, 44, 48] where the angle of a point in the Poincaré disc represents the preferred orientation and its modulus the corresponding selectivity. In this model, radially localized solutions can be interpreted as the analogue of the tuning curves found for the ring model of orientation [14, 58, 95] or the analogue of the tuning surfaces of the spherical model developed by Bressloff and Cowan [16, 19]. We have proved that the neural field model set on the Poincaré disc is able to spontaneously produce radially localized solutions i.e. tuning surfaces. Then, due to the equivariance of equation (2.11) with respect to hyperbolic translations [26, 48], there exists a family of radially localized solutions which are translated copies of the solution given by Theorem 2.2. Each translated copy is a tuning surface with a high activity region centered at some given point in the Poincaré disc. As for the Euclidean case, we found that localized solutions stable to radial perturbations exist in a region of the parameter plane $(\mu, \widetilde{W}_c)$ (the grey region of figure 7($b$)); in the hyperbolic case, the region is significantly smaller. The next step of the analysis would be to introduce into equation (2.11) an external input, weakly tuned to a specific preferred texture, and study if our network is able to produce a tuned response.

A natural extension of this work would be to study the effects of spike frequency adaptation [49, 50, 74] and synaptic depression [22, 64, 65] on spatiotemporal dynamics of

our neural field models, where we expect to find spirals, breathers and traveling waves; we leave this for further work.

Finally, we note that spectral analysis on the real hyperbolic space $\mathbb{H}^n$, $n \geqslant 2$, has received much interest in the areas of quantum chaos [8, 11, 34, 91] and cosmology [62, 75]. More recently, some aspects of dispersive and concentration phenomena have been studied for evolution equations such as the nonlinear Schrödinger equation and the wave equation posed on $\mathbb{H}^n$ [4, 5, 12]. Our study of radial states in (1.1) in this paper constitutes, from a mathematical point of view, a framework to highlight the inherent differences and similarities between the Euclidean and the hyperbolic geometry that may be of interest in other areas of physics.

## Acknowledgments

GF and JR were partially funded by the ERC advanced grant NerVi number 227747 and by the European Union Seventh Framework Program (FP7/2007-2013) under grant agreement no 269921 (BrainScaleS). DL acknowledges support from an EPSRC grant EP/H05040X/1.

## References

[1] Amari S-I 1977 Dynamics of pattern formation in lateral-inhibition type neural fields *Biol. Cybernet.* **27** 77–87
[2] Amari S I 1975 Homogeneous nets of neuron-like elements *Biol. Cybernet.* **17** 211–20
[3] Angelucci A, Levitt J B, Walton E J, Hupe J M, Bullier J and Lund J S 2002 Circuits for local and global signal integration in primary visual cortex *J. Neurosci.* **22** 8633–46
[4] Anker J P and Pierfelice V 2009 Nonlinear schrödinger equation on real hyperbolic spaces *Annales de l'Institut Henri Poincare (C) Non Linear Analysis* vol 26 (Amsterdam: Elsevier) pp 1853–69
[5] Anker J P, Pierfelice V and Vallarino M 2012 The wave equation on hyperbolic spaces *J. Diff. Eqns* **252** 5613–61
[6] Atay F M and Hutt A 2005 Stability and bifurcations in neural fields with finite propagation speed and general connectivity *SIAM J. Appl. Math.* **65** 644–66
[7] Atay F M and Hutt A 2006 Neural fields with distributed transmission speeds and long-range feedback delays *SIAM J. Appl. Dyn. Syst.* **5** 670–98
[8] Aurich R and Steiner F 1989 Periodic-orbit sum rules for the Hadamard–Gutzwiller model *Physica* D **39** 169–93
[9] Avitabile D, Lloyd D J B, Burke J, Knobloch E and Sandstede B 2010 To snake or not to snake in the planar Swift–Hohenberg equation *SIAM J. Appl. Dyn. Syst.* **9** 704
[10] Avitabile D, Lloyd D J B, Ninsuman K, Sandstede B and Yoon D Y 2013 Radial oscillons in two reaction–diffusion models, in preparation
[11] Balazs N L and Voros A 1986 Chaos on the pseudosphere *Phys. Rep.* **143** 109–240
[12] Banica V 2007 The nonlinear Schrödinger equation on hyperbolic space *Commun. Partial Diff. Eqns* **32** 1643–77
[13] Beck M, Knobloch J, Lloyd D J B, Sandstede B and Wagenknecht T 2009 Snakes, ladders and isolas of localized patterns *SIAM J. Math. Anal.* **41** 936–72
[14] Ben-Yishai R, Bar-Or R L and Sompolinsky H 1995 Theory of orientation tuning in visual cortex *Proc. Natl Acad. Sci.* **92** 3844–8
[15] Bigun J and Granlund G 1987 Optimal orientation detection of linear symmetry *Proc. Ist Int. Conf. on Computer Vision* (New York: IEEE Computer Society) pp 433–8
[16] Bressloff P C and Cowan J D 2002 A spherical model for orientation and spatial frequency tuning in a cortical hypercolumn *Phil. Trans. R. Soc.* B **357** 1643–67
[17] Bressloff P C 2012 Spatiotemporal dynamics of continuum neural fields *J. Phys. A: Math. Theor.* **45** 033001
[18] Bressloff P C, Bressloff N W and Cowan J D 2000 Dynamical mechanism for sharp orientation tuning in an integrate-and-fire model of a cortical hypercolumn *Neural Comput.* **12** 2473–511
[19] Bressloff P C and Cowan J D 2002 So(3) symmetry breaking mechanism for orientation and spatial frequency tuning in the visual cortex *Phys. Rev. Lett.* **88** 078102
[20] Bressloff P C, Cowan J D, Golubitsky M and Thomas P J 2001 Scalar and pseudoscalar bifurcations motivated by pattern formation on the visual cortex *Nonlinearity* **14** 739

[21] Bressloff P C, Cowan J D, Golubitsky M, Thomas P J and Wiener M C 2001 Geometric visual hallucinations, euclidean symmetry and the functional architecture of striate cortex *Phil. Trans. R. Soc. Lond.* B **306** 299–330
[22] Bressloff P C and Kilpatrick Z P 2011 Two-dimensional bumps in piecewise smooth neural fields with synaptic depression *SIAM J. Appl. Math.* **71** 379–408
[23] Burke J and Knobloch E 2007 Homoclinic snaking: structure and stability *Chaos* **17** 7102
[24] Burke J and Knobloch E 2007 Snakes and ladders: localized states in the Swift–Hohenberg equation *Phys. Lett.* A **360** 681–8
[25] Chavane F, Sharon D, Jancke D, Marre O, Frégnac Y and Grinvald A 2011 Lateral spread of orientation selectivity in V1 is controlled by intracortical cooperativity *Front. Syst. Neurosci.* **5** at press
[26] Chossat P and Faugeras O 2009 Hyperbolic planforms in relation to visual edges and textures perception *Plos Comput. Biol.* **5** e1000625
[27] Chossat P, Faye G and Faugeras O 2011 Bifurcations of hyperbolic planforms *J. Nonlinear Sci.* **21** 465–98
[28] Chossat P and Lauterbach R 2000 *Methods in Equivariant Bifurcations and Dynamical Systems* (Singapore: World Scientific)
[29] Colby C L, Duhamel J R and Goldberg M E 1995 Oculocentric spatial representation in parietal cortex *Cereb. Cortex* **5** 470–81
[30] Coombes S 2010 Large-scale neural dynamics: simple and complex *NeuroImage* **52** 731–9
[31] Coombes S, Lord G J and Owen M R 2003 Waves and bumps in neuronal networks with axo-dendritic synaptic interactions *Physica D: Nonlinear Phenom.* **178** 219–41
[32] Coombes S 2005 Waves, bumps and patterns in neural fields theories *Biol. Cybernet.* **93** 91–108
[33] Coombes S, Schmidt H and Bojak I 2012 Interface dynamics in planar neural field models *J. Math. Neurosci.* **2** 9
[34] Cornish N J and Turok N G 1998 Ringing the eigenmodes from compact manifolds *Class. Quantum Grav.* **15** 2699
[35] Coullet P, Riera C and Tresser C 2000 Stable static localized structures in one dimension *Phys. Rev. Lett.* **84** 3069–72
[36] Curtu R and Ermentrout B 2004 Pattern formation in a network of excitatory and inhibitory cells with adaptation *SIAM J. Appl. Dyn. Syst.* **3** 191
[37] Doedel E J and Oldeman B 2009 Continuation and bifurcation software for ordinary differential equations *Tech. Report*
[38] Elvin A J, Laing C R, McLachlan R I and Roberts M G 2010 Exploiting the Hamiltonian structure of a neural field model *Physica D: Nonlinear Phenom.* **239** 537–46
[39] Erdelyi A 1985 *Higher Transcendental Functions* vol 1 (Huntington, NY: Robert E Krieger)
[40] Ermentrout G B and Cowan J D 1979 A mathematical theory of visual hallucination patterns *Biol. Cybernet.* **34** 137–50
[41] Ermentrout G B 1998 Neural networks as spatio-temporal pattern-forming systems *Rep. Prog. Phys.* **61** 353–430
[42] Faugeras O, Grimbert F and Slotine J-J 2008 Absolute stability and complete synchronization in a class of neural fields models *SIAM J. Appl. Math.* **61** 205–50
[43] Faye G 2012 Reduction method for studying localized solutions of neural field equations on the Poincaré disc *C. R. Acad. Sci.* **350** 161–6
[44] Faye G 2012 Symmetry breaking and pattern formation in some neural field equations *PhD Thesis* EDSFA
[45] Faye G and Chossat P 2013 A spatialized model of textures perception using structure tensor formalism *Netw. Heterogenous Media* at press
[46] Faye G, Rankin J and Chossat P 2013 Localized states in an unbounded neural field equation with smooth firing rate function: a multi-parameter analysis *J. Math. Biol.* at press
[47] Faye G and Chossat P 2011 Bifurcation diagrams and heteroclinic networks of octagonal H-planforms *J. Nonlinear Sci.* **22** 277–325
[48] Faye G, Chossat P and Faugeras O 2011 Analysis of a hyperbolic geometric model for visual texture perception *J. Math. Neurosci.* **1** 1–51
[49] Folias S E and Bressloff P C 2005 Breathers in two-dimensional neural media *Phys. Rev. Lett.* **95** 208107
[50] Folias S E and Bressloff P C 2004 Breathing pulses in an excitatory neural network *SIAM J. Appl. Dyn. Syst.* **3** 378–407
[51] Funahashi S, Bruce C J and Goldman-Rakic P S 1989 Mnemonic coding of visual space in the monkey's dorsolateral prefrontal cortex *J. Neurophysiol.* **61** 331–49
[52] Golubitsky M, Shiau L J and Török A 2003 Bifurcation on the visual cortex with weakly anisotropic lateral coupling *SIAM J. Appl. Dyn. Syst.* **2** 97–143

[53] Golubitsky M, Stewart I and Schaeffer D G 1988 *Singularities and Groups in Bifurcation Theory* vol 2 (Berlin: Springer)
[54] González B J and Negrin E R 1997 Mehler–Fock transforms of generalized functions via the method of adjoints *Proc. Am. Math. Soc.* **125** 3243–54
[55] Gradshteyn I S and Ryzhik I M 2007 *Table of Integrals, Series and Products* ed A Jeffrey and D Zwillinger (New York: Academic)
[56] Guo Y and Chow C C 2005 Existence and stability of standing pulses in neural networks: I. Existence *SIAM J. Appl. Dyn. Syst.* **4** 217–48
[57] Guo Y and Chow C C 2005 Existence and stability of standing pulses in neural networks: II. Stability *SIAM J. Appl. Dyn. Syst.* **4** 249–81
[58] Hansel D and Sompolinsky H 1997 Modeling feature selectivity in local cortical circuits *Methods Neuronal Modeling* 499–567
[59] Hubel D H and Wiesel T N 1968 Receptive fields and functional architecture of monkey striate cortex *J. Physiol.* **195** 215
[60] Hubel D H and Wiesel T N 1977 Functional architecture of Macaque monkey *Proc. R. Soc. London* B **192** 1–59
[61] Hutt A and Atay F M 2005 Analysis of nonlocal neural fields for both general and gamma-distributed connectivities *Physica D: Nonlinear Phenom.* **203** 30–54
[62] Inoue K T 1999 Computation of eigenmodes on a compact hyperbolic 3-space *Class. Quantum Grav.* **16** 3071
[63] Jirsa V K and Haken H 1996 Field theory of electromagnetic brain activity *Phys. Rev. Lett.* **77** 960–3
[64] Kilpatrick Z P and Bressloff P C 2010 Effects of synaptic depression and adaptation on spatiotemporal dynamics of an excitatory neuronal network *Physica D: Nonlinear Phenom.* **239** 547–60
[65] Kilpatrick Z P and Bressloff P C 2010 Spatially structured oscillations in a two-dimensional excitatory neuronal network with synaptic depression *J. Comput. Neurosci.* **28** 193–209
[66] Kilpatrick Z P, Folias S E and Bressloff P C 2008 Traveling pulses and wave propagation failure in inhomogeneous neural media *SIAM J. Appl. Dyn. Syst.* **7** 161–85
[67] Kishimoto K and Amari S 1979 Existence and stability of local excitations in homogeneous neural fields *J. Math. Biol.* **7** 303–18
[68] Knobloch J, Lloyd D J B, Sandstede B and Wagenknecht T 2011 Isolas of 2-pulse solutions in homoclinic snaking scenarios *J. Dyn. Diff. Eqns* **23** 93–114
[69] Knobloch J and Wagenknecht T 2005 Homoclinic snaking near a heteroclinic cycle in reversible systems *Physica D: Nonlinear Phenom.* **206** 82–93
[70] Knutsson H 1989 Representing local structure using tensors *Scandinavian Conf. on Image Analysis (Oulu, Finland)* pp 244–51
[71] Krauskopf B, Osinga H M and Galán-Vioque J 2007 *Numerical Continuation Methods for Dynamical Systems* (Berlin: Springer)
[72] Laing C R and Troy W C 2003 PDE methods for nonlocal models *SIAM J. Appl. Dyn. Syst.* **2** 487–516
[73] Laing C R, Troy W C, Gutkin B and Ermentrout G B 2002 Multiple bumps in a neuronal model of working memory *SIAM J. Appl. Math.* **63** 62–97
[74] Laing C R 2005 Spiral waves in nonlocal equations *SIAM J. Appl. Dyn. Syst.* **4** 588–606
[75] Lehoucq R, Weeks J, Uzan J-P, Gausmann E and Luminet J-P 2002 Eigenmodes of 3-dimensional spherical spaces and their application to cosmology *Class. Quantum Gravity* **19** 4683–708
[76] Lloyd D J B and O'Farrell H 2013 On localized hotspots of an urban crime model, in preparation
[77] Lloyd D and Sandstede B 2009 Localized radial solutions of the Swift–Hohenberg equation *Nonlinearity* **22** 485
[78] Lloyd D J B, Sandstede B, Avitabile D and Champneys A R 2008 Localized hexagon patterns of the planar Swift–Hohenberg equation *SIAM J. Appl. Dyn. Syst.* **7** 1049–100
[79] Lund J S, Angelucci A and Bressloff P C 2003 Anatomical substrates for functional columns in macaque monkey primary visual cortex *Cerebral Cortex* **12** 15–24
[80] McCalla S 2011 Localized structures in the multi-dimensional Swift–Hohenberg equation *PhD Thesis* Brown University, Providence
[81] McCalla S and Sandstede B 2010 Snaking of radial solutions of the multi-dimensional Swift–Hohenberg equation: a numerical study *Physica D: Nonlinear Phenom.* **239** 1581–92
[82] McCalla S and Sandstede B 2013 Spots in the Swift–Hohenberg equation, in preparation
[83] Miller E K, Erickson C A and Desimone R 1996 Neural mechanisms of visual working memory in prefrontal cortex of the macaque *J. Neurosci.* **16** 5154–67
[84] Orban G A, Kennedy H and Bullier J 1986 Velocity sensitivity and direction selectivity of neurons in areas V1 and V2 of the monkey: influence of eccentricity *J. Neurophysiol.* **56** 462–80

[85] Owen M R, Laing C R and Coombes S 2007 Bumps and rings in a two-dimensional neural field: splitting and rotational instabilities *New J. Phys.* **9** 378–401
[86] Pinto D J and Ermentrout G B 2001 Spatially structured activity in synaptically coupled neuronal networks: I. Traveling fronts and pulses *SIAM J. Appl. Math.* **62** 206–25
[87] Pinto D J and Ermentrout G B 2001 Spatially structured activity in synaptically coupled neuronal networks: II. Standing pulses *SIAM J. Appl. Math.* **62** 226–43
[88] Rubin J E and Troy W C 2004 Sustained spatial patterns of activity in neuronal populations without recurrent excitation *SIAM J. Appl. Math.* **64** 1609–35
[89] Sandstede B 2007 Evans functions and nonlinear stability of traveling waves in neuronal network models *Int. J. Bifurcation Chaos* **17** 2693–704
[90] Scheel A 2003 *Radially Symmetric Patterns Reaction–Diffusion Systems* vol 165 (Providence, RI: American Mathematical Society)
[91] Schmit C 1991 Quantum and classical properties of some billiards on the hyperbolic plane *Chaos Quantum Phys.* pp 335–69
[92] Tass P 1995 Cortical pattern formation during visual hallucinations *J. Biol. Phys.* **21** 177–210
[93] Taylor J G 1999 Neural 'bubble' dynamics in two dimensions: foundations *Biol. Cybernet.* **80** 393–409
[94] Terras A 1988 *Harmonic Analysis on Symmetric Spaces and Applications* vol 2 (Berlin: Springer)
[95] Veltz R 2011 Nonlinear analysis methods in neural field models *PhD Thesis* Univ Paris Est
[96] Virchenko N O and Fedotova I 2001 *Generalized Associated Legendre Functions and their Applications* (Singapore: World Scientific)
[97] Watson G N 1944 *A Treatise on the Theory of Bessel Functions* (Cambridge: Cambridge University Press)
[98] Werner H and Richter T 2001 Circular stationary solutions in two-dimensional neural fields *Biol. Cybernet.* **85** 211–17
[99] Wilson H R and Cowan J D 1972 Excitatory and inhibitory interactions in localized populations of model neurons *Biophys. J.* **12** 1–24
[100] Wilson H R and Cowan J D 1973 A mathematical theory of the functional dynamics of cortical and thalamic nervous tissue *Biol. Cybernet.* **13** 55–80
[101] Woods P D and Champneys A R 1999 Heteroclinic tangles and homoclinic snaking in the unfolding of a degenerate reversible Hamiltonian-Hopf bifurcation *Physica D: Nonlinear Phenom.* **129** 147–70